Phoretic self-propulsion at finite Péclet numbers

Sébastien Michelin[1,†] and Eric Lauga[2]

[1]LadHyX, Département de Mécanique, Ecole Polytechnique – CNRS, 91128 Palaiseau, France

[2]Department of Applied Mathematics and Theoretical Physics, University of Cambridge, Cambridge CB3 0WA, UK

Phoretic self-propulsion is a unique example of force- and torque-free motion on small scales. The classical framework describing the flow field around a particle swimming by self-diffusiophoresis neglects the advection of the solute field by the flow and assumes that the chemical interaction layer is thin compared to the particle size. In this paper we quantify and characterize the effect of solute advection on the phoretic swimming of a sphere. We first rigorously derive the regime of validity of the thin-interaction-layer assumption at finite values of the Péclet number (*Pe*). Under this assumption, we solve computationally the flow around Janus phoretic particles and examine the impact of solute advection on propulsion and the flow created by the particle. We demonstrate that although advection always leads to a decrease of the swimming speed and flow stresslet at high values of the Péclet number, an increase can be obtained at intermediate values of *Pe*. This possible enhancement of swimming depends critically on the nature of the chemical interactions between the solute and the surface. We then derive an asymptotic analysis of the problem at small *Pe* which allows us to rationalize our computational results. Our computational and theoretical analysis is accompanied by a parallel study of the influence of reactive effects at the surface of the particle (Damköhler number) on swimming.

Key words: biological fluid dynamics, low-Reynolds-number flows, swimming/flying

1. Introduction

Self-propulsion at low Reynolds number is usually associated with the biological world. Indeed, many cellular organisms, both prokaryotic and eukaryotic, display some form of motility in fluids (Bray 2000). Since the equations of motion are linear in this regime, the type of motion leading to self-propulsion has to be non-time-reversible (Purcell 1977). This is typically achieved through the actuation of cellular appendages called flagella or cilia which act on a surrounding viscous fluid in a wave-like fashion (Brennen & Winnet 1977; Lauga & Powers 2009).

Beyond the biological world, artificial micro-scale swimmers have received increasing attention in recent years, motivated in part by their potential use in a biomedical context (Nelson, Kaliakatsos & Abbott 2010). The design of most synthetic swimmers to date has been inspired by the biological world, thus attempting

† Email address for correspondence: sebastien.michelin@ladhyx.polytechnique.fr

to reproduce, for example, the two-dimensional beating of a sperm flagellum (Dreyfus *et al.* 2005) or the three-dimensional rotation of a bacterial flagellum (Ghosh & Fischer 2009; Gao *et al.* 2010; Zhang, Peyer & Nelson 2010). In all these cases, the actuation is not embedded in the swimmer itself or the surrounding fluid, but is due to the use of external fields, typically magnetic.

A promising alternative approach to designing truly self-propelled swimmers takes advantage of the short-range interaction between the surface of a colloidal particle and an outer field gradient (e.g. solute concentration, temperature or electric field) to locally create fluid motion in the vicinity of a particle boundary (Anderson 1989). These so-called phoretic mechanisms are responsible for the migration of isotropic particles in externally imposed gradients. Furthermore, they may be exploited to generate self-propulsion when the particle is itself able to generate local gradients, for example through chemical reaction or heat radiation, an idea which has led to significant activity in the physics and chemistry communities (Paxton *et al.* 2004; Golestanian, Liverpool & Ajdari 2005, 2007; Howse *et al.* 2007; Córdova-Figueroa & Brady 2008; Jülicher & Prost 2009*a*; Jiang, Yoshinaga & Sano 2010; Ebbens & Howse 2011). Such swimmers are usually referred to as phoretic.

Physically, when the interaction layer (chemical, electrical, temperature etc.) is thin compared to the particle size, phoretic effects amount to the generation of a distribution of slip velocities at the particle surface (Jülicher & Prost 2009*b*), and can thus be thought of as a biomimetic analogue of propulsion by dense arrays of short beating cilia (Blake 1971). In order to induce non-trivial tangential chemical gradients and slip velocities, anisotropic properties of the particle surface are essential for small particles (Golestanian *et al.* 2005, 2007), and isotropic particles cannot swim unless they are large enough for a symmetry-breaking instability, involving advection of the surrounding chemical field, to take place (Michelin, Lauga & Bartolo 2013). The main advantage of this type of swimmer design is that the particles can swim in the absence of any external field and can thus represent true force-free, torque-free self-propulsion (Wang 2009). The diffusiophoretic propulsion of such solid particles shares many similarities with self-propelled Marangoni droplets, which swim as a result of self-generated gradients of reactive surfactants (Thutupalli, Seemann & Herminghaus 2011; Yoshinaga *et al.* 2012; Schmitt & Stark 2013).

In this paper, we focus on the case of self-diffusiophoresis where the slip velocities are induced through the chemical interactions between a diffusive solute and a particle whose surface acts partly as a catalyst for a chemical reaction. A classical continuum framework has recently been proposed to study the dynamics of an isolated phoretic particle through the coupling of a Stokes flow problem to the diffusing and reacting dynamics of the solute (Golestanian *et al.* 2007). This original framework was based on three main assumptions: (i) the diffuse layer where the solute–particle interaction takes place was assumed to be infinitely thin, so that the phoretic effect can be accounted for by a slip velocity at the surface of the particle; (ii) the advection of the solute was neglected, effectively decoupling the solute diffusion dynamics from the Stokes flow problem; (iii) on the catalyst portion of the particle surface, the chemistry was described by a fixed-rate absorption or release of the solute. In recent years, this framework has been used and extended to study a variety of properties of the self-propulsion of asymmetric colloidal particles, including advective effects (Córdova-Figueroa & Brady 2008; Jülicher & Prost 2009*b*; Córdova-Figueroa, Brady & Shklyaev 2013), the role of geometry (Popescu *et al.* 2010), the impact of more complex surface chemistry (Ebbens *et al.* 2012) and the non-zero thickness of the interaction layer (Sabass & Seifert 2012; Sharifi-Mood, Koplik & Maldarelli 2013).

In the coupled fluid–chemical transport problem, neglecting the advection of the solute significantly simplifies the mathematical analysis, since it effectively decouples the two problems. The solute concentration satisfies a diffusion equation which can be solved first, and its solution can then be exploited in the fluid problem to compute the swimming speed and the flow field. This assumption of zero solute Péclet number, *Pe*, is appropriate when the size of the particle is small enough, when the particle activity or mobility is weak (in some well-defined sense which will be detailed below) or when the solute diffusivity is large. However, advective effects may become significant when the particle is not small compared to $a_c = D/\mathcal{U}$, where D is the solute diffusivity and $\mathcal{U}$ the characteristic phoretic velocity (Jülicher & Prost 2009*b*). This is particularly relevant in the case of large proteins or molecules when D is very small. The catalytic autodegradation of hydrogen peroxide by platinum Janus particles, and the resulting locomotion through gradients of oxygen, corresponds to a critical size $a_c \approx 10$–$100\ \mu$m (Howse *et al.* 2007; Ebbens *et al.* 2012). Large *Pe* values can also be obtained at much smaller scales when the chemical species correspond to larger molecules (such as surfactants; see Thutupalli *et al.* 2011). When *Pe* is no longer negligible, advection of the solute has been shown to significantly impact the velocity of such particles (Jülicher & Prost 2009*b*; Khair 2013; Michelin *et al.* 2013). Furthermore, the validity of the slip-velocity assumption in the presence of strong advective effects needs to be investigated. Solute advection at large values of *Pe* will lead to chemical boundary layers, and not only can advection within the diffuse layer become significant but the diffuse-layer thickness may no longer be negligible compared to the concentration boundary layer.

In addition, most self-diffusiophoresis studies consider either a fixed absorption release of solute at the surface (Golestanian *et al.* 2007; Jülicher & Prost 2009*b*; Sabass & Seifert 2012) or a one-step absorption reaction where the solute flux is proportional to its local concentration (Córdova-Figueroa & Brady 2008). The former approach can be seen as a particular case of the latter where the solute concentration is only weakly affected by the reaction and is still mainly determined by its far-field value, a limit adapted to the case of small particles. The importance of reactive effects, measured by the Damköhler number *Da*, must still be quantified. For large values of *Da*, solute diffusion is too slow to refresh the solute content of the fluid near the surface of the particle, and phoretic effects may be reduced, potentially affecting self-propulsion.

The goal of the present paper is to quantify and characterize the effect of advection and reaction on phoretic self-propulsion. We first introduce the general continuum phoretic model for a spherical particle with arbitrary surface chemical properties. Asymptotic expansions are then exploited to analyse in detail the validity of the thin-interaction-layer limit in the presence of advective and reactive effects. Using this assumption, a mathematical and computational framework is developed for solving the phoretic problem at arbitrary values of *Pe* and *Da* for axisymmetric particles, in particular for Janus particles possessing one chemically active cap while the rest of the particle surface is chemically inert (Walther & Müller 2008). We then use computations to analyse the impact of advection and reaction on the swimming velocity and the flow field induced by the particle motion. We show in particular that advective effects can increase the swimming speed of phoretic swimmers and amplify the flow they induce in the far field. Finally, we use analytical calculations at small *Pe* and *Da* numbers to rigorously calculate the sensitivity to both advection and reaction of arbitrary Janus particles, thereby explaining our computational results.

2. Autophoretic propulsion

The dynamics of an isolated solid particle of radius a is considered in a fluid of density ρ_f and dynamic viscosity η_f. A solute S dispersed in the fluid and characterized by its concentration, $C(\boldsymbol{x}, t)$, interacts with the particle's surface through a short-range potential $\Phi(\boldsymbol{x}) = k_B T \phi(\boldsymbol{x})$ with range λ (i.e. $|\Phi|/k_B T \ll 1$ if $|\boldsymbol{x}| - a \gg \lambda$, where the centre of the coordinate system is taken to be at the centre of the sphere). The solute is characterized by a far-field concentration C_∞ and may be released and/or absorbed at the surface through chemical reaction.

In the following, a general framework is presented that can account for two different types of surface chemistry (Michelin *et al.* 2013): a fixed-flux absorption/release characterized by an activity $\mathscr{A}$; and a fixed-rate one-step chemical reaction $S \rightarrow P$ characterized by a reaction rate $\mathscr{K}$. In the latter case, although both reactant S and product P may interact with the surface, we will neglect for simplicity the interaction with P; but what follows may easily be generalized to account for the chemical interaction of both species with the surface. The chemical properties of the particle surface are then characterized by a distribution of either activity or reaction rate.

The solute S is assumed to diffuse with diffusivity D and to be advected by the fluid flow. In the following, it is assumed that the Reynolds number $Re = \rho_f U a / \eta_f$ is small enough for both fluid and solid inertia to be negligible. If furthermore the particle density is taken to equal that of the fluid, then the particle is force-free and torque-free.

Near the particle, the interaction between the solute in suspension and the particle surface induces a force $-\nabla\Phi$ on a given solute molecule. As a result, the force density applied to the fluid is $-C(\boldsymbol{x})\nabla\Phi$. In a reference frame attached to the centre of the particle, the equations of motion for the fluid flow simplify to the Stokes equations

$$\boldsymbol{0} = -\nabla p + \eta_f \nabla^2 \boldsymbol{u} - C\nabla\Phi, \quad \nabla \cdot \boldsymbol{u} = 0, \qquad (2.1a,b)$$

subject to the far-field condition and the no-slip boundary condition on the particle surface ($r = a$ with $r = |\boldsymbol{x}|$):

$$\boldsymbol{u}(r \rightarrow \infty) \sim -\boldsymbol{U} - \boldsymbol{\Omega} \times \boldsymbol{x}, \quad \boldsymbol{u}(r = a) = \boldsymbol{0}. \qquad (2.2a,b)$$

In (2.2), $\boldsymbol{U}$ and $\boldsymbol{\Omega}$ are, respectively, the unknown translation and rotation velocities of the rigid particle.

The advection–diffusion for the solute is governed by the equation

$$\frac{\partial C}{\partial t} + \nabla \cdot \boldsymbol{j} = 0, \qquad (2.3)$$

where the solute flux $\boldsymbol{j}$ includes advection by the flow, diffusion and transport by the interaction potential in the form

$$\boldsymbol{j} = C\boldsymbol{u} - D\left(\nabla C + \frac{C\nabla\Phi}{k_B T}\right). \qquad (2.4)$$

The solute concentration must also satisfy the far-field condition

$$C(r \rightarrow \infty) \sim C_\infty. \qquad (2.5)$$

Finally, the chemical properties of the particle surface control the surface flux. Denoting by x^S a point on the surface of the particle, we have

$$Dn \cdot \left(\nabla C + \frac{C\nabla\Phi}{k_B T} \right)\bigg|_{(|x^S|=a)} = \begin{cases} -\mathscr{A}(x^S), & \text{fixed-flux}; \\ \mathscr{K}(x^S)C, & \text{fixed-rate}. \end{cases} \tag{2.6}$$

In the fixed-flux case, positive activity corresponds to an emission of solute while negative activity corresponds to absorption. The one-step chemical reaction with fixed rate always corresponds to an absorption and hence can be seen as a negative activity depending on the local concentration. Note that we assume the basic mechanism of absorption/desorption of the reactant/product on the surface catalyst to be fast enough that the solute concentration on the surface is at equilibrium with its immediate fluid environment at all times.

This set of equations for $\{C, u, p\}$ and (U, Ω) is closed by imposing the force- and torque-free conditions on the particle:

$$\iint_{r=a} \sigma \cdot n \, dS + \iiint_{\Omega_f} C\nabla\Phi \, d\Omega = 0, \tag{2.7}$$

$$\iint_{r=a} x \times (\sigma \cdot n) \, dS + \iiint_{\Omega_f} x \times (C\nabla\Phi) \, d\Omega = 0. \tag{2.8}$$

In (2.7), the total force applied to the particle is the sum of the hydrodynamic force, with stress tensor $\sigma = -p\mathbf{1} + \eta_f(\nabla u + \nabla u^{\mathrm{T}})$, and the interaction forces with the solute in the entire fluid domain. Since the solute–surface interaction is of short range, this is approximately equivalent to imposing conditions of zero hydrodynamic force and torque on any surface outside the interaction layer, e.g. a sphere of radius $R \gtrsim \lambda + a$.

The fixed-rate and fixed-flux approaches can be combined into a single framework by solving for $c = C - C_\infty$ instead of C. The advection–diffusion problem is now written as

$$\frac{\partial c}{\partial t} + u \cdot \nabla c = D\nabla \cdot \left(\nabla c + \frac{(c + C_\infty)\nabla\Phi}{k_B T} \right), \tag{2.9}$$

$$c(r \to \infty) \to 0 \tag{2.10}$$

and

$$Dn \cdot \left(\nabla c + \frac{(c + C_\infty)\nabla\Phi}{k_B T} \right) = -\mathscr{A}^* + \mathscr{K}c \quad \text{for } |x^S| = a. \tag{2.11}$$

The fixed-flux approach is obtained with $\mathscr{K} = 0$ and $\mathscr{A}^* = \mathscr{A}$, while for the fixed-rate approach $\mathscr{K} \neq 0$ and $\mathscr{A}^* = -\mathscr{K}C_\infty$.

The problem is non-dimensionalized using a as the characteristic length. Since c is the concentration distribution relative to the far-field value, its characteristic variations scale with the normal gradients imposed at the surface by chemistry. A natural scale for c is therefore $[c] = \mathcal{A}a/D$ where $\mathcal{A}$ is the typical magnitude of the modified activity (given either by the magnitude of $\mathscr{A}(x^S)$ or by $\mathcal{K}C_\infty$ with $\mathcal{K}$ the magnitude of $\mathscr{K}$). A characteristic scale for the velocity u is obtained from the dominant balance in the diffuse layer between viscous diffusion and solute–surface interactions and is chosen as $[U] = k_B T \lambda^2 [c]/\eta_f a$, from which the characteristic pressure is obtained as

$k_B T[c](\lambda/a)^2$ and the characteristic time as $a/[U]$. The phoretic propulsion problem above now becomes, in dimensionless form,

$$\nabla^2 \boldsymbol{u} - \nabla p = \frac{(c + c_\infty)\nabla\phi}{\varepsilon^2}, \quad \nabla \cdot \boldsymbol{u} = 0, \tag{2.12a,b}$$

$$Pe\left(\frac{\partial c}{\partial t} + \boldsymbol{u} \cdot \nabla c\right) = \nabla \cdot \left(\nabla c + (c + c_\infty)\nabla\phi\right), \tag{2.13}$$

$$c(r \to \infty) \to 0, \quad \boldsymbol{u}(r \to \infty) \sim -(\boldsymbol{U} + \boldsymbol{\Omega} \times \boldsymbol{x}), \tag{2.14a,b}$$

$$\boldsymbol{u}|_{|\boldsymbol{x}^S|=1} = \boldsymbol{0}, \quad \boldsymbol{n} \cdot [\nabla c + (c + c_\infty)\nabla\phi]_{|\boldsymbol{x}^S|=1} = k(\boldsymbol{x}^S) + Da\, k(\boldsymbol{x}^S)c, \tag{2.15a,b}$$

and is characterized by four non-dimensional numbers:

$$Pe = \frac{k_B T \mathcal{A} \lambda^2 a}{\eta_f D^2}, \quad Da = \frac{\mathcal{K}a}{D}, \quad \varepsilon = \frac{\lambda}{a}, \quad c_\infty = \frac{DC_\infty}{\mathcal{A}a}. \tag{2.16a,b,c,d}$$

Note that in (2.15), $k(\boldsymbol{x}^S)$ is defined as $-\mathscr{A}^*/\mathcal{A}$ for both the fixed-flux and fixed-rate problems. The Péclet number, Pe, is the ratio of diffusive to advective time scales; the Damköhler number, Da, is the ratio of diffusive to reactive time scales; ε is the dimensionless range of the interaction potential; and c_∞ is the ratio of the far-field concentration to the typical variations of concentrations around the particle. Note that the equations above are valid even when ε is not small. In the next section, we consider the classical thin-layer limit, $\varepsilon \ll 1$, for finite values of both Pe and Da.

3. The thin-interaction-layer limit and its limitations

Most studies on self-diffusiophoresis focus on the $\varepsilon \ll 1$ limit of short-range potentials, when the solute–particle interactions are restricted to a thin boundary layer around the particle (Golestanian *et al.* 2005, 2007). In this thin-interaction-layer limit, all phoretic effects are bundled into two boundary conditions applied to the outer boundary of the interaction layer, which is identical to the particle surface in the limit $\varepsilon \ll 1$, namely a slip velocity due to tangential solute gradients and a normal solute flux imposed by the chemistry at the particle surface. In this section, we revisit this limit of short-range potential $\varepsilon \ll 1$, in order to investigate the validity of that framework when neither advection (Pe) nor reaction (Da) can be neglected. Diffusiophoresis shares several fundamental properties and mechanisms with other phoretic phenomena (Anderson 1989), and it should be noted that the 'thin interaction layer' analysis discussed below has many similarities to the 'thin Debye layer' limit considered in classical work on electrophoresis (O'Brien 1983; Prieve *et al.* 1984). Recently, the study of Yariv (2010) proposed a detailed analysis of the asymptotic regime in the case of electrophoresis of particles in externally imposed electric fields.

The main result of this section is to show that the validity conditions for each of the boundary conditions above correspond to two distinct mathematical limits. First, in the limit $\varepsilon^2 Pe \ll 1$, the flow outside the interaction layer can be solved for by taking into account a slip velocity $\boldsymbol{u}^S$ at the boundary, given by

$$\boldsymbol{u}^S = M(\boldsymbol{I} - \boldsymbol{nn}) \cdot \nabla c, \tag{3.1}$$

with the local mobility M defined from the local interaction potential profile. If additionally we have $\varepsilon Pe \ll 1$, then advection within the interaction layer is negligible, and the solute advection–diffusion outside this interaction layer can be solved for

independently of the interaction-layer dynamics by applying to the outer boundary of this layer the flux condition imposed by the chemistry at the particle surface.

Since we have $\varepsilon \ll 1$, in order for both results to be valid we need to be in the limit $\varepsilon Pe \ll 1$. In the rest of § 3 we present the technical derivation of these two conditions, and readers who are mostly interested in the particle dynamics may skip these derivations, retaining only the two conclusions above. Note that the derivations and results presented in this section are valid regardless of the surface properties of the spherical particle (activity and interaction potential). In particular, they are applicable to both axisymmetric and non-axisymmetric distributions. In the following, $\zeta = (\theta, \phi)$ will generically stand for the two angular coordinates in spherical polar coordinates and will be used to characterize this angular (and not necessarily axisymmetric) dependence of the particle's properties.

The derivations below follow the classical approach of matched asymptotic expansions (Bender & Orszag 1978), distinguishing between an outer solution, obtained for $r - 1 = O(1)$ in the region where solute–particle interactions are negligible, and an inner solution, obtained for $\rho = (r - 1)/\varepsilon = O(1)$ in the interaction layer (Brady 2011; Sabass & Seifert 2012; Sharifi-Mood *et al.* 2013).

3.1. *Outer solution*

Expanding all outer fields in the form of a regular expansion in ε, $f = f_0(r, \zeta) + \varepsilon f_1(r, \zeta) + \cdots$, and provided that $\phi_0 = \phi_1 = 0$, which is expected for all classical interaction potentials decaying at least as fast as $1/(r-1)^2$, at leading order the outer problem becomes

$$\nabla^2 \boldsymbol{u}_0 - \boldsymbol{\nabla} p_0 = \boldsymbol{0}, \quad \boldsymbol{\nabla} \cdot \boldsymbol{u}_0 = 0, \tag{3.2a,b}$$

$$Pe \left(\frac{\partial c_0}{\partial t} + \boldsymbol{u}_0 \cdot \boldsymbol{\nabla} c_0 \right) = \nabla^2 c_0, \tag{3.3}$$

$$c_0(r \to \infty) \to 0, \quad \boldsymbol{u}_0(r \to \infty) \sim -\boldsymbol{U}_0 - \boldsymbol{\Omega}_0 \times \boldsymbol{x}, \tag{3.4a,b}$$

and is identical to other advection–diffusion problems in Stokes flow, such as the feeding of model ciliates (Michelin & Lauga 2011, 2013). First-order corrections in ε (namely all f_1 quantities) satisfy the exact same equations. For both problems, the boundary conditions at $r = 1$ must be obtained through matching with the inner solution by expanding the different fields for $r - 1 \ll 1$ as

$$f(r, \zeta) = f_0(1, \zeta) + (r - 1) \frac{\partial f_0}{\partial r}(1, \zeta) + \varepsilon f_1(1, \zeta) + o\big((r - 1), \varepsilon\big). \tag{3.5}$$

3.2. *Inner solution*

We now focus on the inner problem for $\rho = (r - 1)/\varepsilon = O(1)$. Defining $\tilde{\phi}(\rho, \zeta) = \phi((r-1)/\varepsilon, \zeta)$, we can write $\tilde{\phi}$ as a regular expansion in ε,

$$\tilde{\phi}(\rho, \zeta) = \tilde{\phi}_0(\rho, \zeta) + \varepsilon \tilde{\phi}_1(\rho, \zeta) + \cdots, \tag{3.6}$$

and the same expansion can be carried out for the inner concentration $\tilde{c}$ as well as all velocity components. Anticipating the dominant balance in the momentum equations, the inner pressure is expanded as

$$\tilde{p}(r, \mu) = \frac{\tilde{p}_0}{\varepsilon^2} + \frac{\tilde{p}_1}{\varepsilon} + \tilde{p}_2 + \cdots. \tag{3.7}$$

Note that this difference of scaling between the inner and outer pressures imposes that $\tilde{p}_i(r \to \infty) \to 0$ for $i = 0, 1$.

We now substitute these expansions into the Stokes equations (2.12). Keeping only the first two dominant terms, the equations can be rewritten as

$$\frac{\partial \tilde{u}_{r0}}{\partial \rho} + \varepsilon \left[\frac{\partial \tilde{u}_{r1}}{\partial \rho} + 2\tilde{u}_{r0} + \boldsymbol{\nabla} \cdot \tilde{\boldsymbol{u}}_{\|0} \right] = O(\varepsilon^2), \tag{3.8}$$

$$\frac{\partial \tilde{p}_0}{\partial \rho} + (c_\infty + \tilde{c}_0) \frac{\partial \tilde{\phi}_0}{\partial \rho} + \varepsilon \left[\frac{\partial \tilde{p}_1}{\partial \rho} + (c_\infty + \tilde{c}_0) \frac{\partial \tilde{\phi}_1}{\partial \rho} + \tilde{c}_1 \frac{\partial \tilde{\phi}_0}{\partial \rho} - \frac{\partial^2 \tilde{u}_{r0}}{\partial \rho^2} \right] = O(\varepsilon^2), \tag{3.9}$$

$$\frac{\partial^2 \tilde{\boldsymbol{u}}_{\|0}}{\partial \rho^2} - \boldsymbol{\nabla}_\| \tilde{p}_0 - (c_\infty + \tilde{c}_0) \boldsymbol{\nabla}_\| \tilde{\phi}_0 + \varepsilon \left[\frac{\partial^2 \tilde{\boldsymbol{u}}_{\|1}}{\partial \rho^2} + 2 \frac{\partial \tilde{\boldsymbol{u}}_{\|0}}{\partial \rho} - \boldsymbol{\nabla}_\| \tilde{p}_1 - \tilde{c}_1 \boldsymbol{\nabla}_\| \tilde{\phi}_0 \right.$$

$$\left. - (c_\infty + \tilde{c}_0) \boldsymbol{\nabla}_\| \tilde{\phi}_1 + \rho \boldsymbol{\nabla}_\| \tilde{p}_0 + \rho(c_\infty + \tilde{c}_0) \boldsymbol{\nabla}_\| \tilde{\phi}_0 \right] = O(\varepsilon^2), \tag{3.10}$$

with $\boldsymbol{u}_\| = (\boldsymbol{I} - \boldsymbol{e}_r \boldsymbol{e}_r) \cdot \boldsymbol{u}$ and $\boldsymbol{\nabla}_\| p = (\boldsymbol{I} - \boldsymbol{e}_r \boldsymbol{e}_r) \cdot \boldsymbol{\nabla} p$. Similarly, the advection–diffusion problem for the inner concentration $\tilde{c}$ can be rewritten as

$$\frac{\partial}{\partial \rho} \left(\frac{\partial \tilde{c}_0}{\partial \rho} + (c_\infty + \tilde{c}_0) \frac{\partial \phi_0}{\partial \rho} \right) + \varepsilon \left[\frac{\partial}{\partial \rho} \left(\frac{\partial \tilde{c}_1}{\partial \rho} + \tilde{c}_1 \frac{\partial \phi_0}{\partial \rho} + (c_\infty + \tilde{c}_0) \frac{\partial \phi_1}{\partial \rho} \right) \right.$$

$$\left. + 2 \left(\frac{\partial \tilde{c}_0}{\partial \rho} + (c_\infty + \tilde{c}_0) \frac{\partial \tilde{\phi}_0}{\partial \rho} \right) \right]$$

$$= \varepsilon Pe \, \tilde{u}_{r0} \frac{\partial \tilde{c}_0}{\partial \rho} + \varepsilon^2 Pe \left(\tilde{u}_{r1} \frac{\partial \tilde{c}_0}{\partial \rho} + \tilde{\boldsymbol{u}}_{\|0} \cdot \boldsymbol{\nabla}_\| \tilde{c}_0 \right) + O(\varepsilon^2, \varepsilon^3 Pe), \tag{3.11}$$

with the boundary condition at the sphere surface, (2.15), becoming

$$\frac{\partial \tilde{c}_0}{\partial \rho} + (c_\infty + \tilde{c}_0) \frac{\partial \tilde{\phi}_0}{\partial \rho} + \varepsilon \left[\frac{\partial \tilde{c}_1}{\partial \rho} + (c_\infty + \tilde{c}_0) \frac{\partial \tilde{\phi}_1}{\partial \rho} + \tilde{c}_1 \frac{\partial \tilde{\phi}_0}{\partial \rho} \right] = \varepsilon k(\zeta)(1 + Da \, \tilde{c}_0) + O(\varepsilon^2) \tag{3.12}$$

at $\rho = 0$.

At leading order, mass conservation, (3.8), imposes that $\partial \tilde{u}_{r0}/\partial \rho = 0$. Together with the impermeability condition at the particle boundary, this shows that

$$\tilde{u}_{r0}(\rho, \zeta) = 0. \tag{3.13}$$

At leading order, the momentum conservation equations in the radial and azimuthal directions, (3.9) and (3.10), lead to

$$\frac{\partial \tilde{p}_0}{\partial \rho} + (c_\infty + \tilde{c}_0) \frac{\partial \tilde{\phi}_0}{\partial \rho} = 0, \tag{3.14}$$

$$\frac{\partial^2 \tilde{\boldsymbol{u}}_{\|0}}{\partial \rho^2} - \boldsymbol{\nabla}_\| \tilde{p}_0 - (c_\infty + \tilde{c}_0) \boldsymbol{\nabla}_\| \tilde{\phi}_0 = \boldsymbol{0}. \tag{3.15}$$

Provided that $\varepsilon^2 Pe \ll 1$, (3.11) and (3.12) can be solved to leading order as

$$\tilde{c}_0(\rho, \zeta) = -c_\infty + \mathcal{C}_0(\zeta) \, e^{-\tilde{\phi}_0(\rho, \zeta)}. \tag{3.16}$$

Substitution of this result into (3.14), together with the decay condition of $\tilde{p}_0$ and $\tilde{\phi}_0$ for $\rho \gg 1$, leads to

$$\tilde{p}_0(\rho, \zeta) = \mathcal{C}_0(\zeta)(e^{-\tilde{\phi}_0(\rho,\zeta)} - 1). \tag{3.17}$$

Finally, substituting this result into (3.15), we obtain after integration and rearrangement that

$$\tilde{\boldsymbol{u}}_{\|0}(\rho, \zeta) = -\boldsymbol{\nabla}_{\|}\mathcal{C}_0 \left[\int_0^\infty R \left(e^{-\tilde{\phi}_0(R,\zeta)} - 1 \right) \mathrm{d}R + \int_\rho^\infty (\rho - R) \left(e^{-\tilde{\phi}_0(R,\zeta)} - 1 \right) \mathrm{d}R \right] + \boldsymbol{\beta}\rho, \tag{3.18}$$

where $\mathcal{C}_0(\zeta)$ and $\boldsymbol{\beta}(\zeta)$ are to be determined through matching with the outer solution.

3.3. *Matching at leading order and slip velocity*

Matching the outer and inner solutions at leading order shows that $\boldsymbol{\beta} = 0$ and gives the following relations:

$$c_0(1, \zeta) = \mathcal{C}_0(\zeta) - c_\infty, \tag{3.19}$$
$$u_{r0}(1, \zeta) = 0, \tag{3.20}$$
$$\boldsymbol{u}_{\|0} = M(\zeta)\boldsymbol{\nabla}_{\|}\mathcal{C}_0, \tag{3.21}$$

with M, the mobility coefficient, given by

$$M(\zeta) = -\int_0^\infty \rho \left(e^{-\tilde{\phi}_0(\rho,\zeta)} - 1 \right) \mathrm{d}\rho. \tag{3.22}$$

Combining (3.20) and (3.21), we therefore establish that, provided $\varepsilon^2 Pe \ll 1$, the outer problem can be solved at leading order using a slip boundary condition

$$\boldsymbol{u} = M(\boldsymbol{I} - \boldsymbol{nn}) \cdot \boldsymbol{\nabla}c \tag{3.23}$$

at $r = 1$, characterized by the mobility coefficient $M(\zeta)$ in (3.22) (Anderson 1989). For locally attractive interactions ($\phi_0 < 0$) the mobility coefficient is negative and the slip velocity is oriented down-gradient, while for locally repulsive interactions ($\phi_0 > 0$) the slip velocity is oriented in the direction of the tangential solute gradient.

3.4. *Validity of the flux condition*

Since the flux boundary condition in (2.15) does not appear at leading order, the slip velocity result, (3.23), is not sufficient to close the outer system formed by (3.2)–(3.4). In order to obtain the additional boundary condition on c_0, it is necessary to carry out the expansion in the inner region to the next order (see also the work of Yariv 2010 for a similar treatment in the case of electrophoresis). Provided $\varepsilon Pe \ll 1$, the next-order contribution to the advection–diffusion equation and boundary condition, (3.11) and (3.12), leads to

$$\frac{\partial \tilde{c}_1}{\partial \rho} + \tilde{c}_1 \frac{\partial \tilde{\phi}_0}{\partial \rho} = -(c_\infty + \tilde{c}_0)\frac{\partial \tilde{\phi}_1}{\partial \rho} + k(\zeta) + Da\,k(\zeta)\tilde{c}_0. \tag{3.24}$$

After integration, we obtain

$$\tilde{c}_1(\rho, \zeta) = e^{-\tilde{\phi}_0(\rho,\zeta)}\Bigg[\mathcal{C}_1(\zeta) + \rho k(\zeta)\Big(1 + Da\,(\mathcal{C}_0(\zeta) - c_\infty)\Big)$$
$$+ k(\zeta)(Da\,c_\infty - 1)\int_\rho^\infty \Big(e^{\tilde{\phi}_0(R,\zeta)} - 1\Big)\,\mathrm{d}R - \mathcal{C}_0(\zeta)\tilde{\phi}_1\Bigg]. \qquad (3.25)$$

Using the previous equation and (3.16), in the limit of $\rho \gg 1$ and $\varepsilon \ll 1$ we have

$$\tilde{c} = \mathcal{C}_0(\zeta) - c_\infty + \varepsilon\rho\,[k(\zeta) + Da\,k(\zeta)\,(\mathcal{C}_0 - c_\infty)] + \varepsilon\mathcal{C}_1(\mu) + o(\varepsilon, \varepsilon\rho). \qquad (3.26)$$

Upon matching with the expansion of the outer solution c for $(r - 1) \ll 1$, (3.5), we obtain

$$\frac{\partial c_0}{\partial r}(1, \zeta) = k(\zeta) + Da\,k(\zeta)c_0(1, \zeta). \qquad (3.27)$$

This equation simply states that the diffusive flux at the outer boundary of the interaction layer is equal to the diffusive flux at the particle surface. In this limit, advection is negligible in the interaction layer and the solute simply diffuses in the radial direction. This provides the missing boundary condition for $(\boldsymbol{u}_0, c_0)$ and leads to an autonomous and well-posed set of equations.

This condition breaks down, however, when advection within the diffuse layer becomes important and $\varepsilon Pe = O(1)$ or, equivalently, when $k_B T \mathcal{A}\lambda^3/\eta_f D^2 = O(1)$. That condition does not depend on the size a of the phoretic particle, only on the surface properties and diffusivity coefficients. Current experimental applications correspond to interaction layers of typical thickness $\lambda \lesssim 1$ nm (Howse *et al.* 2007; Ebbens *et al.* 2012), so that $\varepsilon = O(10^{-5}\text{–}10^{-3})$ for micrometric particles, and therefore advective effects within the interaction layer are indeed negligible, even for $Pe = O(1)$.

Note that even in the absence of advective effects in the outer region ($Pe = 0$), advective effects within the interaction layer may modify significantly the diffusive flux when the interaction potential is strong enough for the adsorption length to be comparable to the particle's size (Anderson & Prieve 1991). Such effects are implicitly neglected here: our choice for the scaling of the flow velocity within the interaction layer assumes that the adsorption length and interaction-layer thickness are comparable.

To conclude, it is noteworthy that the validity conditions for the two approximations resulting from the thin-diffuse-layer framework, namely the slip velocity and the boundary flux of solute, are mathematically different at high Pe, i.e. $\varepsilon \ll Pe^{-1/2}$ for the slip velocity definition versus $\varepsilon \ll Pe^{-1}$ for the boundary flux of solute.

4. Self-propulsion of autophoretic Janus particles at finite Péclet and Damköhler numbers

In §§ 4–6, we present a model for the autophoretic self-propulsion of axisymmetric particles based on the above approximations and investigate the effect of Pe on the self-propulsion properties of autophoretic particles. We assume that ε is sufficiently small such that the limit $\varepsilon Pe \ll 1$ allows us to consider intermediate and large values of Pe. In that limit, the solute–particle interactions are entirely accounted for by a slip velocity, (2.15), and a flux condition, (3.1), both valid at the particle's outer limit ($r = 1^+$).

Focusing on steady-state propulsion, the resulting phoretic problem is expressed as

$$\nabla^2 \boldsymbol{u} - \nabla p = \boldsymbol{0}, \quad \nabla \cdot \boldsymbol{u} = 0, \tag{4.1a,b}$$

$$Pe\, \boldsymbol{u} \cdot \nabla c = \nabla^2 c, \tag{4.2}$$

$$c(r \to \infty) \to 0, \quad \boldsymbol{u}(r \to \infty) \sim -(\boldsymbol{U} + \boldsymbol{\Omega} \times \boldsymbol{x}), \tag{4.3a,b}$$

and

$$\frac{\partial c}{\partial r}(r = 1) = k(\zeta)(1 + Da\, c), \quad \boldsymbol{u}(r = 1) = M(\zeta)(\boldsymbol{I} - \boldsymbol{nn}) \cdot \nabla c. \tag{4.4a,b}$$

The swimming velocity and rotation rate are obtained using the reciprocal theorem for a force-free and torque-free particle (Stone & Samuel 1996) and are given by

$$\boldsymbol{U} = -\frac{1}{4\pi} \int_{r=1} \boldsymbol{u}_\parallel \, \mathrm{d}S, \quad \boldsymbol{\Omega} = -\frac{3}{8\pi} \int_{r=1} \boldsymbol{n} \times \boldsymbol{u}_\parallel \, \mathrm{d}S. \tag{4.5a,b}$$

The problem now depends only on two dimensionless parameters, *Da* and *Pe*. The Damköhler number *Da* characterizes the importance of diffusion in controlling the surface kinetics of the solute. When $Da = 0$, diffusion is fast enough for the absorption of solute to be controlled by its far-field concentration and to be essentially independent of the local fluctuations of solute concentration (fixed-flux framework). In contrast, for finite *Da*, the concentration fluctuations resulting from the absorption of solute at the interface are significant. The Péclet number *Pe* characterizes the relative importance of the influences of advection and diffusion on the solute distribution. When $Pe = 0$, the flow resulting from phoretic effects at the particle surface has no impact on the solute distribution. Both non-dimensional numbers can also be seen as measures of the particle size, and the classical framework ($Pe = Da = 0$) is therefore appropriate for small particles. Here we investigate the advective and reactive effects when the particle size is no longer small enough for both *Pe* and *Da* to be neglected.

For simplicity, we focus exclusively on the absorption of a solute through chemical reaction ($k > 0$); the 'release' problem is easily obtained from our results by changing *M* to $-M$. We also assume in the main text that the mobility is uniform, i.e. that the interaction potential is isotropic around the sphere, $\phi(\boldsymbol{x}) = \phi(|\boldsymbol{x}|)$. However, as we show in appendix A, our framework can also be used in the case of non-uniform mobility, and leads to a generalization of the results presented in the main text to arbitrary mobility distributions. Finally, we note that the magnitude of *M* effectively determines the characteristic velocity outside the diffuse layer. Therefore, it is more relevant to rescale the velocity (and pressure) so as to include the effect of the potential distribution. The characteristic velocity scale is now

$$[U] = \frac{k_B T \lambda^2 [c]}{\eta_f a} \left| \int_0^\infty \rho \left(\mathrm{e}^{-\tilde{\phi}_0(\rho)} - 1 \right) \mathrm{d}\rho \right|, \tag{4.6}$$

so that the non-dimensional mobility is simply $M = \pm 1$.

4.1. *The axisymmetric phoretic problem*

From (4.5), we see that a sufficient condition for the self-propulsion of a phoretic particle relies on the particle's ability to generate a slip velocity field at its surface with a non-zero average. As the slip velocity originates from local solute gradients, one natural way to create self-propulsion is to consider non-isotropic particles with a reactive cap on an otherwise inert surface. Tangential gradients in solute

concentrations are then expected to be generated between inert and active regions, leading to slip velocity and locomotion. These so-called Janus particles are typically axisymmetric and have been the focus of most experimental, theoretical and numerical studies on autophoretic particles (Golestanian *et al.* 2005, 2007; Córdova-Figueroa & Brady 2008; Jülicher & Prost 2009*b*; Jiang *et al.* 2010; Sabass & Seifert 2012).

For such axisymmetric particles, the chemical properties of the surface are characterized by an activity $k = k(\mu)$ with $\mu = \cos\theta$, where θ is the polar angle with respect to the axis of symmetry $\boldsymbol{e}_z$ in spherical polar coordinates. The solute concentration and the flow field are also axisymmetric, and we write $c = c(r, \mu)$ and $\boldsymbol{u} = u_r(r, \mu)\boldsymbol{e}_r + u_\theta(r, \mu)\boldsymbol{e}_\theta$. Consequently, the motion of the particle is a pure translation along $\boldsymbol{e}_z$, $\boldsymbol{U} = U\boldsymbol{e}_z$, with no rotation, i.e. $\boldsymbol{\Omega} = 0$.

In this setting, the Stokes flow problem can be solved explicitly using the squirmer formulation (Blake 1971; Michelin & Lauga 2011). The flow velocity is completely determined by the stream function ψ, obtained as the superposition of orthogonal modes,

$$\psi(r, \mu) = \sum_{n=1}^{\infty} \frac{2n+1}{n(n+1)} \alpha_n \psi_n(r)(1-\mu^2)L_n'(\mu), \quad (4.7)$$

where $L_n(\mu)$ is the nth Legendre polynomial and

$$\psi_1(r) = \frac{1-r^3}{3r}, \quad \psi_n(r) = \frac{1}{2}\left(\frac{1}{r^n} - \frac{1}{r^{n-2}}\right) \quad (n \geqslant 2). \quad (4.8a,b)$$

The intensities of the squirming modes, α_n, are obtained through projection of the slip velocity $u_\theta(1, \mu)$ as

$$\alpha_n = \tfrac{1}{2} \int_{-1}^{1} \sqrt{1-\mu^2}\, L_n'(\mu) u_\theta(1, \mu)\, \mathrm{d}\mu. \quad (4.9)$$

The first squirming mode, α_1, is the only mode contributing to the swimming velocity of the particle, so that $\boldsymbol{U} = \alpha_1 \boldsymbol{e}_z$. The second squirming mode, α_2, includes the slowest-decaying contribution to the flow field, namely that of a symmetric force dipole of intensity $\Sigma = 10\pi\alpha_2$. The contribution of this particle to the bulk stress takes the form of a stresslet $\boldsymbol{\Sigma} = \Sigma(\boldsymbol{pp} - \boldsymbol{I}/3)$ (Batchelor 1970). For $\Sigma > 0$ ($\alpha_2 > 0$) this flow field is equivalent to a so-called puller swimmer swimming flagella first (such as the alga *Chlamydomonas*), while $\Sigma < 0$ ($\alpha_2 < 0$) corresponds to a pusher swimming body first (such as most flagellated bacteria and spermatozoa).

With this formalism, the flow field is completely characterized and determined by the intensities of the squirming modes, $\{\alpha_n\}_n$. Decomposing the surface reaction rate $k(\mu)$ and the solute distribution $c(r, \mu)$ into Legendre polynomials,

$$k(\mu) = \sum_{p=0}^{\infty} k_p L_p(\mu), \quad c(r, \mu) = \sum_{p=0}^{\infty} c_p(r) L_p(\mu), \quad (4.10a,b)$$

we can then rewrite the phoretic problem (4.1)–(4.2) as a set of nonlinearly coupled ODEs for the functions $c_p(r)$ ($p \geqslant 0$), from which the characteristics of the flow field can be retrieved. Specifically, we obtain

$$\frac{\mathrm{d}}{\mathrm{d}r}\left(r^2 \frac{\mathrm{d}c_p}{\mathrm{d}r}\right) - p(p+1)c_p = Pe \sum_{n=1}^{\infty} \sum_{m=0}^{\infty} \alpha_n \left[A_{mnp}\psi_n \frac{\mathrm{d}c_m}{\mathrm{d}r} + B_{mnp}\frac{\mathrm{d}\psi_n}{\mathrm{d}r}c_m\right], \quad (4.11)$$
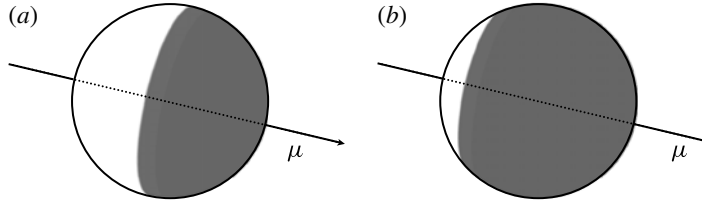
FIGURE 1. The Janus particles A and B considered in our computations: (*a*) particle A is a hemispheric Janus particle with one half inert (white) and one half active (grey); (*b*) particle B is a non-symmetric Janus swimmer with a large reactive pole (grey) and a small inert area (white).

$$c_p(\infty) = 0, \tag{4.12}$$

$$\frac{\mathrm{d}c_p}{\mathrm{d}r}(1) = k_p + Da \sum_{m=0}^{\infty} \sum_{n=0}^{\infty} \frac{A_{mnp}k_n}{2n+1} c_m(1), \tag{4.13}$$

$$\alpha_n = -\frac{n(n+1)M}{2n+1} c_n(1) \quad (n \geqslant 1), \tag{4.14}$$

where the third-order tensors A_{mnp} and B_{mnp} are defined from the Legendre polynomials as (Michelin & Lauga 2011)

$$A_{mnp} = \frac{(2p+1)(2n+1)}{2} \int_{-1}^{1} L_m(\mu)L_n(\mu)L_p(\mu) \, \mathrm{d}\mu, \tag{4.15}$$

$$B_{mnp} = \frac{(2p+1)(2n+1)}{2n(n+1)} \int_{-1}^{1} (1-\mu^2)L_m'(\mu)L_n'(\mu)L_p(\mu) \, \mathrm{d}\mu. \tag{4.16}$$

4.2. *Janus particles*

The Janus particles considered here consist of a reactive cap at one pole of the sphere while the rest of the particle is inert. A variety of Janus particles are considered here which differ by the ratio of their inert to active surface areas (figure 1). The chemical activity distribution is given by $k(\mu) = 1_{\{\mu > \mu_c\}}$, where μ_c denotes the angular size of the active region ($-1 \leqslant \mu_c \leqslant 1$). We assume for simplicity that the phoretic mobility is uniform ($M = \pm 1$); however, this assumption does not impact our main results, which may easily be generalized to Janus mobility distributions such that $M(\mu) = \pm k(\mu)$, as shown in appendix A. For the choice $k(\mu) = 1_{\{\mu > \mu_c\}}$, the spectral coefficients k_n of the activity distribution can be obtained by projection of $k(\mu)$ onto the Legendre polynomials, to give

$$k_0 = \frac{1 - \mu_c}{2}, \quad k_n = \tfrac{1}{2}\left[L_{n-1}(\mu_c) - L_{n+1}(\mu_c)\right] \quad (n \geqslant 1). \tag{4.17a,b}$$

In the limit where both advective and reactive effects can be neglected ($Pe = Da = 0$), the diffusive problem for c, (4.11)–(4.13), can be solved analytically along each azimuthal component, and we obtain

$$c_p(r) = -\frac{k_p}{(p+1)r^{p+1}}. \tag{4.18}$$

Then, (4.14) provides the squirming mode intensities

$$\alpha_p = \frac{p\, k_p M}{2p+1},$$

(4.19)

from which the entire flow field can be computed; in particular, the reference swimming velocity and stresslet, hereafter referred to as U_0 and Σ_0, are obtained as

$$U_0 = \frac{k_1 M}{3} = \frac{M}{4}(1-\mu_c^2), \qquad \Sigma_0 = 4\pi M k_2 = 5\pi M \mu_c (1-\mu_c^2).$$

(4.20a,b)

For our computations in §5, we focus specifically on two such Janus particles, referred to as particles A and B (figure 1) of uniform mobility $M = \pm 1$; this effectively amounts to four different configurations, or two pairs.

Particle A is a hemispheric (symmetric) Janus swimmer ($\mu_c = 0$) with one half chemically active and the other half inert. The corresponding spectral coefficients k_n are computed as

$$k_0^A = \tfrac{1}{2}, \qquad k_{2q}^A = 0, \qquad k_{2q-1}^A = (-1)^{q+1}\frac{4q-1}{4q-2}\frac{(2q)!}{\left[2^q q!\right]^2} \quad (q \geqslant 1).$$

(4.21a,b,c)

In particular, $k_1^A = 3/4$ and $k_2^A = 0$, so that $U_0^A = M/4$ and $\Sigma_0^A = 0$. This is the particle with maximum swimming velocity in the limit where both advective and reactive effects are negligible ($Pe = Da = 0$). The sharpest concentration gradients are located near the equator for particle A, resulting in the largest slip velocities located on an extended surface and oriented mostly horizontally, as illustrated in figure 2(a,c). In contrast, particle A has no stresslet in the $Pe = Da = 0$ limit, and its far-field signature has a faster decay and is dominated by a source dipole and a force quadrupole.

Particle B is a non-symmetric Janus swimmer with $\mu_c = -1/\sqrt{3}$. It consists of a larger active cap and a small inert portion. Using (4.17), one obtains that $k_1^B = 1/2$ and $k_2^B = 5/(6\sqrt{3})$, so that for particle B, we get a smaller swimming velocity, $U_0^B = M/6$, and a finite stresslet, $\Sigma_0^B = -10\pi M/(3\sqrt{3})$. The front between reactive and inert regions is located closer to the pole, and thus involves a smaller share of the particle surface creating slip velocities inclined away from the direction of motion and therefore a smaller swimming speed; see figure 2(b,d). On the other hand, particle B corresponds to a maximum stresslet intensity for $Pe = Da = 0$, and as such is one of the Janus particles inducing the largest far-field hydrodynamic interactions with other particles.

Note that for both particles, the chemical reaction at the surface results in a reduction of the solute concentration near the reactive pole ($\mu = 1$). For a slip velocity oriented along (respectively, against) the surface gradient, i.e. $M = 1$ (respectively, $M = -1$), the slip velocity is oriented from the reactive to the inert pole (respectively, from the inert pole to the reactive pole), resulting in a positive (respectively, negative) swimming velocity.

4.3. *Numerical solution*

For finite values of *Da* and *Pe*, the phoretic problem, (4.11)–(4.14), is solved numerically for each particle. The different azimuthal modes of the solute distribution, $c_p(r)$, are discretized on a stretched radial grid (Michelin & Lauga 2011, 2013), and the iterative process described below is followed.
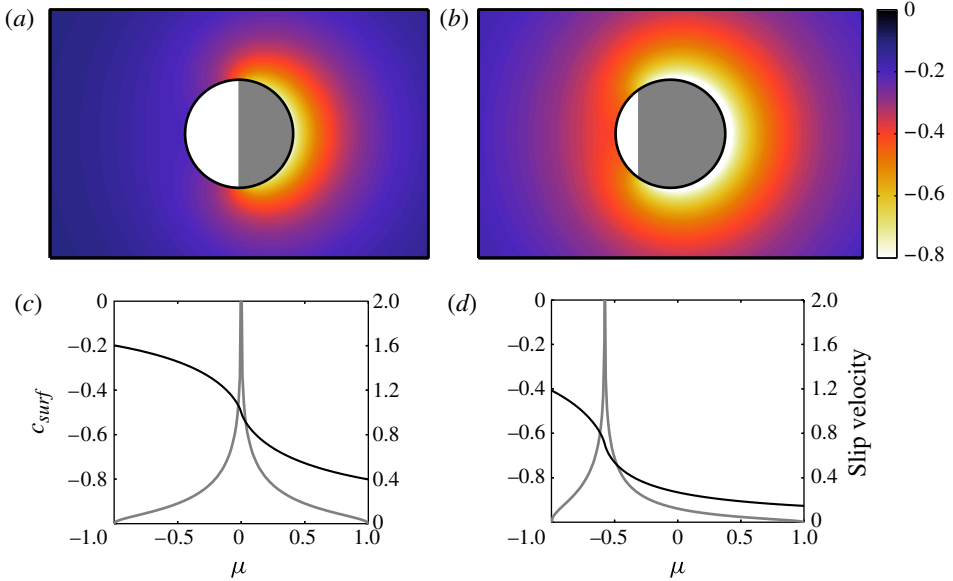
FIGURE 2. (Colour online) (*a,b*) Relative solute concentration distribution, *c*, in the reference configuration with no advective or reactive effects ($Pe = Da = 0$) for: (*a*) Janus particle A, with $|U_0| = 1/4$; (*b*) Janus particle B, with $|U_0| = 1/6$. The reactive cap is shown in grey and the inert portion in white. For $M = 1$ the swimming velocity is oriented to the right, and for $M = -1$ the swimming velocity is oriented to the left. (*c,d*) Surface solute concentration (black) and slip velocity (grey) along the surface in the case of positive mobility ($M = 1$) for: (*c*) particle A; (*d*) particle B.

(i) For an initial guess of the flow, determined by an initial guess of $\{\alpha_n^i\}_n$, the linear advection–diffusion problem, (4.11)–(4.13), is solved directly for $\{c_p(r)\}_p$ (Michelin & Lauga 2011).

(ii) Using the solution of this advection–diffusion problem, (4.14) is used to obtain an updated estimate of the squirming mode intensities, $\{\alpha_n^f\}_n$.

(iii) Broyden's method is used to solve iteratively the nonlinear system $\boldsymbol{F}(\boldsymbol{\alpha}) = \boldsymbol{\alpha}^f - \boldsymbol{\alpha}^i$: knowing an estimate $\boldsymbol{\alpha}^n$ of the solution and an estimate of the inverse of the Jacobian matrix $\boldsymbol{J}_n^{-1} = [\nabla_{\boldsymbol{\alpha}} \boldsymbol{F}(\boldsymbol{\alpha}^n)]^{-1}$, a new estimate for both quantities is obtained as (Broyden 1965)

$$\boldsymbol{\alpha}^{n+1} = \boldsymbol{\alpha}^n - \boldsymbol{J}_n^{-1} \cdot \boldsymbol{\alpha}^n, \tag{4.22}$$

$$\boldsymbol{J}_{n+1}^{-1} = \boldsymbol{J}_n^{-1} + \frac{(\Delta\boldsymbol{\alpha} - \boldsymbol{J}_n^{-1}\Delta\boldsymbol{F}) \cdot (\Delta\boldsymbol{\alpha}^{\mathrm{T}} \cdot \boldsymbol{J}_n^{-1})}{\Delta\boldsymbol{\alpha}^{\mathrm{T}} \cdot \boldsymbol{J}_n^{-1} \cdot \Delta\boldsymbol{\alpha}}, \tag{4.23}$$

where $\boldsymbol{\alpha}^{\mathrm{T}}$ is the transpose of the column vector $\boldsymbol{\alpha}$, $\Delta\boldsymbol{\alpha} = \boldsymbol{\alpha}^{n+1} - \boldsymbol{\alpha}^n$ and $\Delta\boldsymbol{F} = \boldsymbol{F}(\boldsymbol{\alpha}^{n+1}) - \boldsymbol{F}(\boldsymbol{\alpha}^n)$. The iteration is initiated using either a previous computation or the reference solution ($Da = Pe = 0$), in which case the Jacobian matrix must be computed numerically for the initial step.

The number and position of the points on the radial grid, as well as the number of azimuthal modes used for the solute concentration distribution, are adjusted according to the value of the Péclet number (Magar, Goto & Pedley 2003; Michelin & Lauga
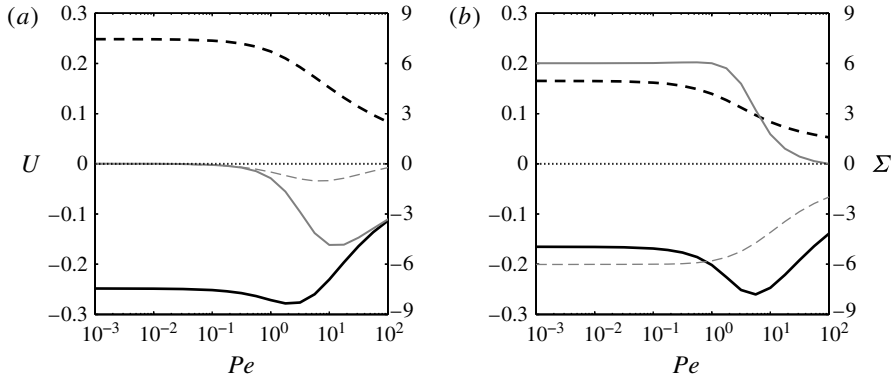
FIGURE 3. Dependence on the value of *Pe* of the swimming velocity (*U*, black lines) and stresslet magnitude (Σ, grey lines) for (*a*) particle A and (*b*) particle B in the fixed-flux limit ($Da = 0$). In each panel, results are shown for both negative mobility $M = -1$ (solid lines) and positive mobility $M = 1$ (dashed lines).

2011). Typical computations for moderate *Pe* include 120 azimuthal modes and 150 radial points. Truncation must also be introduced in the number of squirming modes used and the number of azimuthal components retained for $k(\mu)$. In the results presented below, typically $n_\alpha = 8$ squirming modes were used, as well as $n_k = 12$ modes for the surface activity. These two parameters critically impact computational cost. Convergence tests performed showed that for *Pe* less than 100, the swimming velocity was only marginally affected (less than 0.5 %) when n_α or n_k was doubled.

5. Advective and reactive effects on the self-propulsion of Janus particles

Using the model and formalism presented in §4, we now investigate the effect of advection (*Pe*) and reaction (*Da*) on the self-propulsion of Janus phoretic particles. The asymmetry of the particles ensures that self-propulsion is achieved for all values of *Pe* and *Da*, even in the purely diffusive regime $Pe = Da = 0$. Note that self-propulsion can also be achieved by isotropic or symmetric particles through an instability in the nonlinear advective coupling of solute dynamics to the phoretic flow around the particle (Michelin *et al.* 2013). In that case, and under certain conditions, a critical *Pe* exists above which symmetry-breaking leads to propulsion.

5.1. *Advective effect for the fixed-flux limit (Da = 0)*

We start by considering the effect of advection on phoretic locomotion. When *Pe* is increased, the solute concentration distribution around the particle is modified due to advection of the solute by the flow resulting from the phoretic slip velocity. As a result, local concentration gradients and the slip velocity distribution are also affected, and changes in the swimming velocity occur. For both Janus particles A and B, and for both values of the mobility ($M = \pm 1$), figure 3 shows the dependence of the swimming velocity *U* and the stresslet intensity Σ on the Péclet number *Pe*, in the absence of reactive effects ($Da = 0$). This situation corresponds therefore to a fixed-flux solute absorption at the surface. The case of a fixed-flux solute release is obtained directly by changing *M* to $-M$.

At large values of *Pe*, when advection dominates over solute diffusion, the magnitude of the swimming velocity is seen to always decrease for both particles. Analysis of the numerical data in figure 3 suggests that both $|U|, |\Sigma| \sim Pe^{-1/3}$ at large *Pe*. This scaling is consistent with that suggested by Jülicher & Prost (2009*b*) and can be recovered from dimensional analysis as follows. At large *Pe*, the solute distribution resulting from the advection–diffusion problem is characterized by a boundary layer. The boundary layer thickness δ is the typical length scale associated with radial gradients of the solute concentration, while the typical length scale associated with tangential gradients remains $O(1)$ (i.e. the radius of the spherical particle). The boundary layer thickness δ is then obtained by balancing normal diffusive flux ($\sim \mathcal{C}/\delta^2$) with tangential advection ($\sim Pe\,\mathcal{U}\mathcal{C}$) near the surface, leading to $\delta \sim (Pe\,\mathcal{U})^{-1/2}$, with $\mathcal{U}$ being the typical slip velocity (Michelin & Lauga 2011). When $Da = 0$, the normal diffusive flux is fixed and $O(1)$, and therefore $\mathcal{C} \sim \delta$ is the typical scale of variation of the solute concentration at the surface. Finally, the definition of the phoretic slip velocity in (3.1) imposes that $\mathcal{C} \sim \mathcal{U}$. Combining these three scaling arguments leads to $\mathcal{U}, \mathcal{C}, \delta \sim Pe^{-1/3}$, and the same dependence on *Pe* is recovered for the swimming velocity and stresslet intensity.

Although the autophoretic velocity decreases for all particles with the same scaling at large *Pe*, their finite-*Pe* evolutions differ strongly depending on the sign of the mobility. Particles A and B with positive mobility ($M = 1$) swim in the direction of their active pole (i.e. to the right in figures 1 and 2), and their velocity decreases monotonically in magnitude for all *Pe*. In contrast, particles with negative mobility ($M = -1$) swim towards their inert pole (i.e. to the left), and their velocity varies non-monotonically, reaching a maximum magnitude at $Pe \approx 2$, before decreasing as $Pe^{-1/3}$. The existence of this velocity maximum is a new and notable result, which is not restricted to this type of swimmer. Indeed, several different particle activity distributions were tested, leading to the same result. For any given activity distribution $k(\mu)$, if the velocity magnitude of a particle of mobility M decreases monotonically with *Pe*, then for a particle with the same activity but opposite mobility $-M$, the velocity magnitude shows a peak in magnitude at intermediate values of *Pe*. For Janus particles, our simulations indicate in fact that regardless of the coverage of the active cap (i.e. for all μ_c), particles with negative mobility experience a velocity peak at intermediate *Pe*, while particles with positive mobility exhibit a velocity that decreases monotonically with *Pe*.

For Janus particles, this difference in behaviour depending on the sign of the mobility can be qualitatively understood by comparing the solute concentration distribution around the particles (see figures 4 and 5) with the reference situation at $Pe = 0$ (figure 2). For all particles and all *Pe*, the chemical reaction near the active pole ($\mu = 1$) results in a zone of depletion of the solute concentration in that region. When the particle swims toward the inert pole ($M = -1$, figure 4*c*,*d*), advection of the fluid along the surface tends to concentrate this depleted zone in a narrower region in the wake of the particle. Most importantly, advection brings to the vicinity of the front pole (here the inert one) fluid with higher solute content. Both effects exacerbate the concentration contrast between the fore and aft poles and the solute gradients along the surface, resulting in an increase in the slip and swimming velocity magnitudes when *Pe* is increased (figures 5 and 6). Note that the increase in slip velocity is limited to the reactive region. The slip velocity in the inert region remains roughly identical to the reference configuration. For absorbing particles with negative mobility (or equivalently for emitting particles with positive mobility), the advection of the solute by the phoretic flows introduces a positive feedback on the swimming
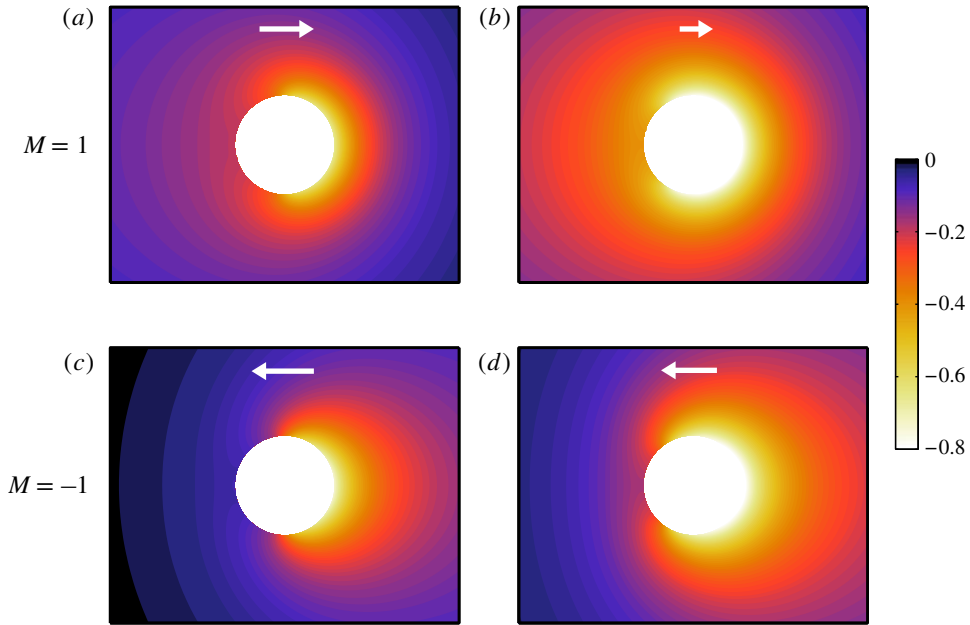
FIGURE 4. (Colour online) Relative concentration distribution c, for $Pe = 2$ and $Da = 0$, around: (*a,c*) phoretic particle A; (*b,d*) phoretic particle B. The swimming velocity of each particle is indicated by a white arrow: (*a*) $U = 0.21$; (*b*) $U = 0.12$; (*c*) $U = -0.28$; (*d*) $U = -0.23$. The reactive part of the surface is shown in grey.
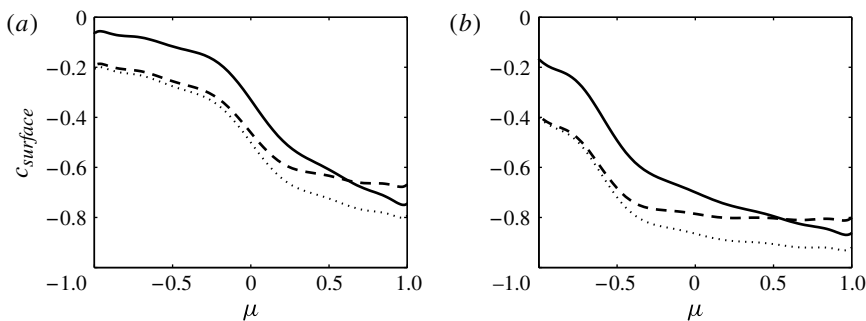

FIGURE 5. Surface concentration distribution for (*a*) particle A and (*b*) particle B, for $Pe = 2$ and $Da = 0$, in the cases of positive mobility ($M = 1$, dashed lines) and negative mobility ($M = -1$, solid lines); the distribution in the reference configuration, $Pe = Da = 0$, is shown as a dotted line in each panel.

velocity, similar to the feedback identified by Michelin *et al.* (2013) on isotropic particles and responsible, in that case, for symmetry-breaking and propulsion. The similarity between these two problems is further discussed in § 6.

In contrast, when the particle swims toward the reactive pole ($M = 1$, figure 4*a,b*), the advection of richer fluid towards the reactive pole tends to increase the concentration in this depleted region, which is also spread over a larger part of the particle by the tangential advection along the surface. This time both effects tend to reduce the concentration contrast between fore and aft poles, resulting in a
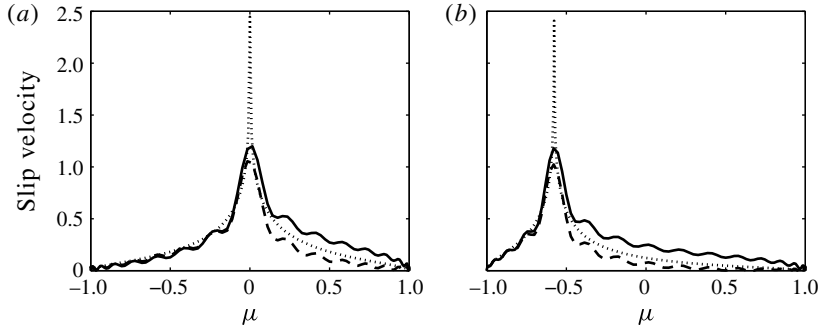
FIGURE 6. Surface slip velocity distribution for (*a*) particle A and (*b*) particle B, for $Pe = 2$ and $Da = 0$, in the cases of positive mobility ($M = 1$, dashed lines) and negative mobility ($M = -1$, solid lines); the slip velocity in the reference configuration, $Pe = Da = 0$, is shown as a dotted line in each panel. Note that due to the computational cost, only 32 modes were used to describe the slip velocity for $Pe = 2$, while the slip velocity in the reference configuration can be obtained analytically from (4.18) and (4.19).

reduction of the slip and swimming velocity magnitudes (figure 6); in this case solute advection by phoretic flows leads to a negative feedback.

When $Pe \gg 1$, however, advection tends to homogenize the solute concentration near the boundary except in a narrow wake region: regardless of the sign of mobility and the swimming direction, advective effects eventually penalize phoretic propulsion.

This difference in behaviour (i.e. existence of an extremum versus monotonic decrease) is also observed for the stresslet, Σ, when $\Sigma_0 \neq 0$ (particle B). However, the magnitude of the peak differs only marginally from the stresslet amplitude in the reference configuration ($|(\Sigma_{max} - \Sigma_0)/\Sigma_0| \approx 0.9\,\%$), so that it is barely visible in figure 3. For Janus particle A, $\Sigma_0 = 0$ when $Pe = 0$ by symmetry, and the stresslet magnitude Σ is always negative for $Pe > 0$ and $Da = 0$. The influence of the phoretic particle on the far-field flow is that of a pusher swimmer, similar to most flagellated bacteria. For both particles, the stresslet magnitude is maximal for $Pe = O(10)$. These results are confirmed and extended to arbitrary Janus particles in §6.

5.2. *Reactive effects in the diffusive limit* ($Pe = 0$)

We now consider the effect of reaction kinetics on the swimming velocity when advective effects are neglected ($Pe = 0$). At finite values of Da, the rate of solute absorption becomes dependent on the local solute concentration. The reaction at the surface is fast enough for diffusion to be unable to maintain a relatively homogeneous background concentration of solute around the particles. In other words, the concentration changes induced by surface reaction are now of similar magnitude to the background/far-field concentration. As a result, the reaction rate will be reduced in regions where the solute concentration is lower, in particular near the active pole.

The dependence of the velocity and stresslet intensity on Da is shown in figure 7. In contrast to the evolution of these quantities with solute advection, we observe a strong symmetry between the cases of positive and negative mobility: in the absence of any advective effects, solute concentration is determined purely by diffusion and has the same distribution regardless of the mobility of the particle. Particles of opposite mobilities have exactly opposite slip velocity distributions. Also, no peak in
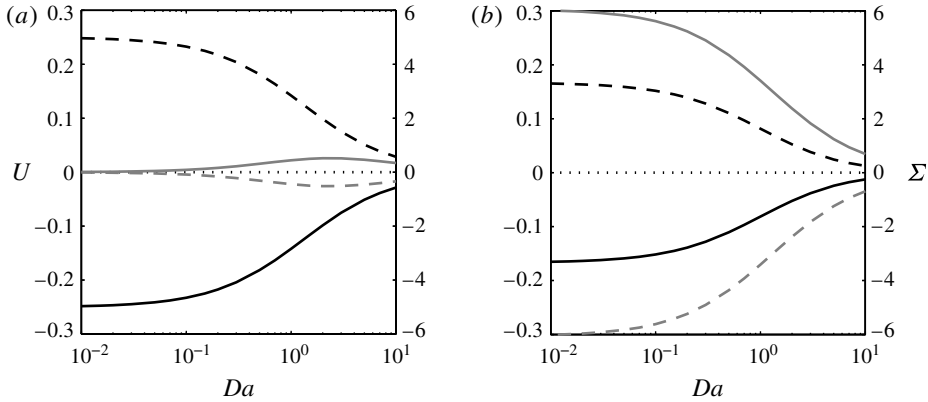
FIGURE 7. Dependence of the swimming velocity (U, black lines) and stresslet magnitude (Σ, grey lines) on Da for (a) particle A and (b) particle B in the diffusive limit ($Pe = 0$). Results are obtained for both negative mobility ($M = -1$, solid lines) and positive mobility ($M = 1$, dashed lines).
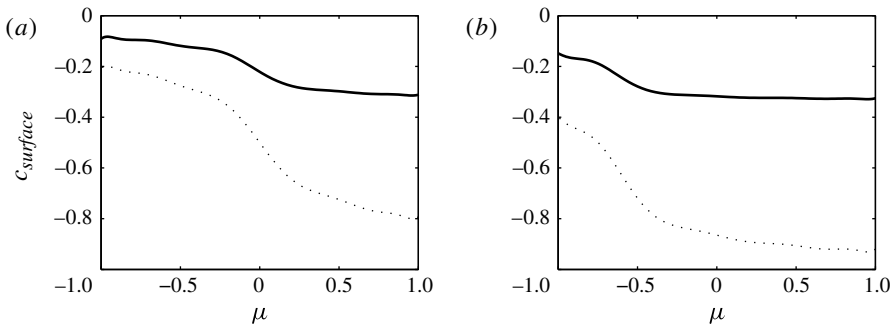

FIGURE 8. Surface concentration distribution (solid lines) for (a) particle A and (b) particle B, for $Da = 2$ and $Pe = 0$. Because advective effects are neglected, the concentration distribution is the same for both $M = 1$ and $M = -1$. The distribution in the reference configuration, $Pe = Da = 0$, is shown as a dotted line in each panel.

the velocity magnitude can be observed. Instead, the swimming velocity decreases monotonically with Da and tends to zero in the limit $Da \gg 1$. This is consistent with the comment above on the roles of diffusion versus reaction. Indeed, for larger values of Da, the reaction leading to the absorption of the solute is slowed down near the active pole (where the solute concentration is lowest), as illustrated in figure 8. As a result, the tangential concentration gradients are reduced and so are the slip and swimming velocities, regardless of the value of the mobility M. In the limit of $Da \gg 1$, a decrease of the swimming velocity as Da^{-1} is observed. In that limit, the diffusion time scale is infinite, leading to a complete depletion of the most reactive regions. The perturbations to the solute concentration on the surface of the particle thus scale as $c \sim -Da^{-1}$, resulting in a similar scaling for the slip and swimming velocities.
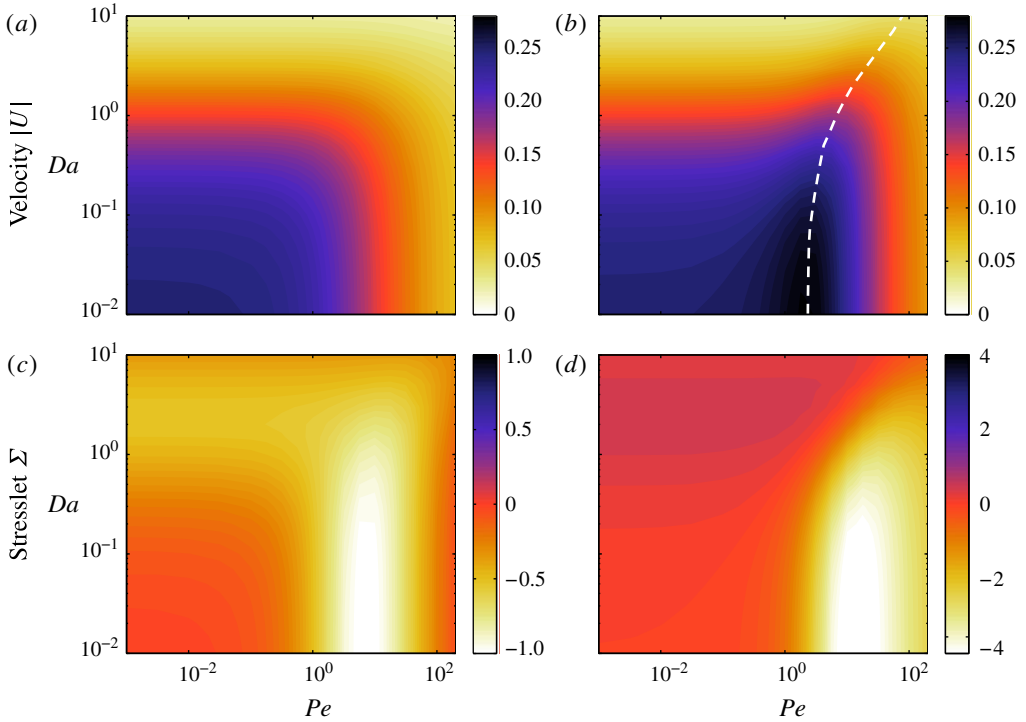
FIGURE 9. (Colour online) Dependence on *Pe* and *Da* of: (*a*) the magnitude of the propulsion velocity, $|U|$, for Janus particle A with $M = 1$; (*b*) the magnitude of the propulsion velocity, $|U|$, for particle A with $M = -1$; (*c*) the stresslet intensity Σ for particle A with $M = 1$; (*d*) the stresslet intensity Σ for particle A with $M = -1$. The white dashed line in panel (*b*) indicates the evolution with *Da* of the optimal *Pe* for which the velocity magnitude is maximal at fixed *Da*.

5.3. *Finite Péclet and Damköhler numbers*

We show in figure 9 the dependence of both U and Σ on finite values of *Pe* and *Da*, and confirm the results obtained in the limits $Pe = 0$ and $Da = 0$. Regardless of the value of the Péclet number, the swimming velocity magnitude is observed to decrease monotonically with *Da*. Further, regardless of the value of the Damköhler number, the dependence of the swimming velocity on *Pe* is different for particles with positive and negative mobilities. The swimming velocity of particles with positive mobility decreases monotonically, while that of particles with negative mobility shows a maximum value for an intermediate *Pe*. Note also that the optimal *Pe* leading to this velocity maximum appears to be an increasing function of *Da*.

6. Sensitivity of arbitrary Janus particles to advective and reactive effects

In the previous section, the effects of advection (*Pe*) and reaction (*Da*) on the swimming velocity and stresslet intensity of two particular Janus particles were investigated computationally. In particular, it was shown that: (i) advection may increase the magnitude of the self-propulsion, when the particle is swimming towards its inert pole at $Pe = 0$; (ii) reactive effects ($Da > 0$) always penalize self-propulsion; and (iii) advective effects create a negative stresslet on particle A (for which $\Sigma_0 = 0$),

resulting in a pusher swimmer. In this section, we first confirm these results and then extend them to more general surface coverage using asymptotic analysis in the limit of $(Pe, Da) \ll 1$. In particular, the sensitivities of the swimming velocity and stresslet to advective and reactive effects are mathematically determined by analytical calculations of four partial derivatives. For arbitrary Pe, the evolution of the swimming velocity and stresslet intensity for arbitrary Janus particles is then addressed numerically.

6.1. *Asymptotic analysis for the autophoretic velocity*

From (4.11)–(4.14), we note that advective effects (Pe) and reactive effects (Da) are responsible for the coupling of the different azimuthal modes. In the limit where $Da = Pe = 0$, the different modes decouple and the solution is obtained explicitly as

$$\bar{c}_p(r) = -\frac{k_p}{(p+1)r^{p+1}}, \quad \bar{\alpha}_p = \frac{pk_pM}{2p+1}. \tag{6.1a,b}$$

Defining the corrections $c'_p = c_p - \bar{c}_p$ and $\alpha'_p = \alpha_p - \bar{\alpha}_p$ to this reference solution, using

$$A_{mn1} = \frac{3(n+1)}{2n+3}\delta_{m,n+1} + \frac{3n}{2n-1}\delta_{m,n-1}, \tag{6.2}$$

$$B_{mn1} = \frac{3(n+2)}{2n+3}\delta_{m,n+1} + \frac{3(n-1)}{2n-1}\delta_{m,n-1} \tag{6.3}$$

and keeping only the linear terms in the correction quantities, (4.11)–(4.13) become, for the swimming mode ($p=1$),

$$\frac{d}{dr}\left(r^2\frac{dc'_1}{dr}\right) - 2c'_1 = Pe\,\bar{\alpha}_1\left[k_0\left(\frac{1}{r^3}-1\right) + \frac{3k_2}{5r^5}\right]$$
$$+ \frac{3Pe}{2}\sum_{n=2}^{\infty}\bar{\alpha}_n\left[k_{n+1}\left(\frac{2n+1}{(2n+3)r^{2n+3}} - \frac{2n-1}{(2n+3)r^{2n+1}}\right)\right.$$
$$\left. + k_{n-1}\left(\frac{1}{r^{2n+1}} - \frac{2n^2-3n+2}{n(2n-1)r^{2n-1}}\right)\right], \tag{6.4}$$

$$c'_1(\infty) = 0, \tag{6.5}$$

$$\frac{dc'_1}{dr}(1) = -Da\sum_{n=0}^{\infty}\frac{3k_nk_{n+1}}{(2n+1)(n+2)}. \tag{6.6}$$

Using (6.1) and solving for $c'_1(r)$, we finally obtain the following expansion at small Pe and Da:

$$U = \frac{k_1M}{3} + Pe\,M^2H_1 + Da\,MH_2 + o(Da, Pe), \tag{6.7}$$

where H_1 and H_2 are constants that depend solely on the details of the surface activity distribution $k(\mu)$ as

$$H_1 = -\frac{k_1k_0}{12} + \frac{k_1k_2}{90} + \sum_{n=2}^{\infty}\frac{(4n-1)k_nk_{n+1}}{(2n+1)(2n+2)(2n+3)(2n+4)}, \tag{6.8}$$
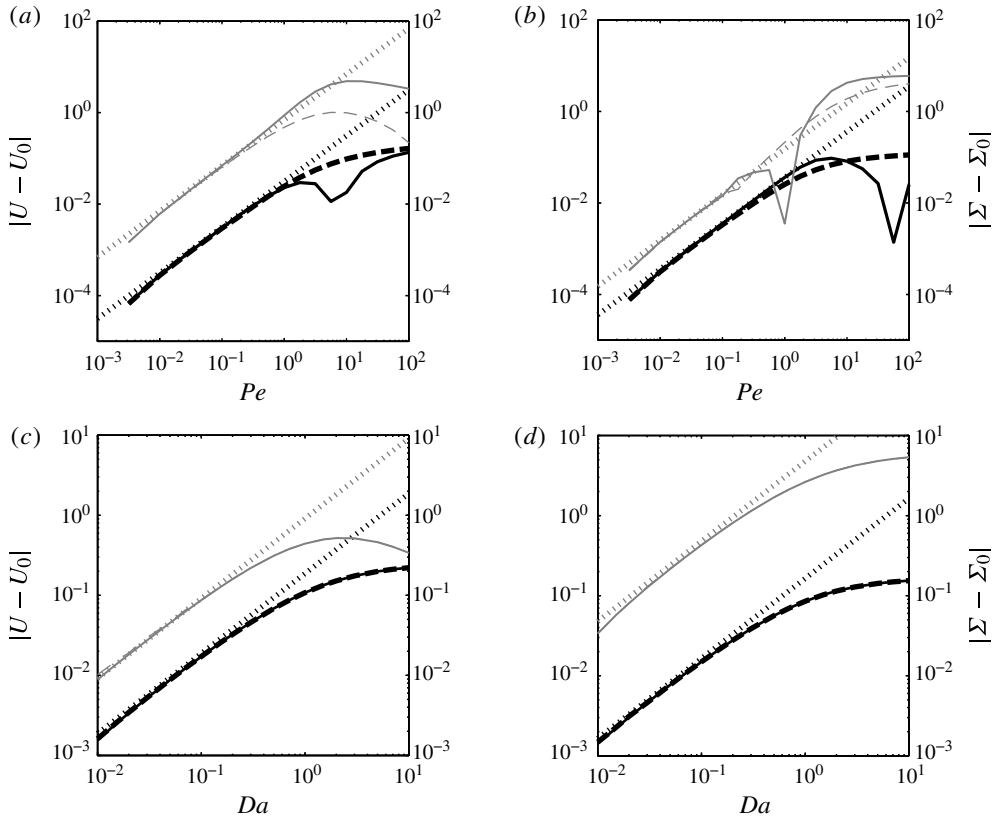
FIGURE 10. Comparison of the numerical results from §5 with the asymptotic predictions in the *Pe, Da* ≪ 1 case for (*a,c*) particle A and (*b,d*) particle B: (*a,b*) evolution of $|U - U_0|$ (black lines) and $|\Sigma - \Sigma_0|$ (grey lines) with *Pe* for *Da* = 0, where U_0 and Σ_0 are the phoretic velocity and stresslet intensity in the absence of advective or reactive effects; (*c,d*) evolution of the same quantities with *Da* for *Pe* = 0. In all panels, solid lines correspond to particles with negative mobility, and dashed lines correspond to particles with positive mobility; the dotted lines correspond to the predictions of (6.7) and (6.11).

$$H_2 = -\sum_{n=0}^{\infty} \frac{k_n k_{n+1}}{(n+2)(2n+1)}. \tag{6.9}$$

Specifically, the sensitivity of the velocity to reactive (*Pe*) and advective (*Da*) effects is obtained as

$$\left(\frac{1}{U}\frac{\partial U}{\partial Pe}\right)_{(Pe,Da)=(0,0)} = \frac{3MH_1}{k_1}, \quad \left(\frac{1}{U}\frac{\partial U}{\partial Da}\right)_{(Pe,Da)=(0,0)} = \frac{3H_2}{k_1}, \tag{6.10a,b}$$

and $k_1 > 0$ by convention for all Janus particles considered (with reactive cap on the right).

This asymptotic prediction shows excellent agreement with the results obtained in §5 for particles A and B (see figure 10). For an arbitrary Janus particle, $k(\mu) = 1_{[\mu_c,1]}$, the evolution of H_1 and H_2 with the size of the reactive cap (measured by $-1 \leqslant \mu_c \leqslant 1$) is shown in figure 11. For all Janus particles, H_1 and H_2 are always negative,
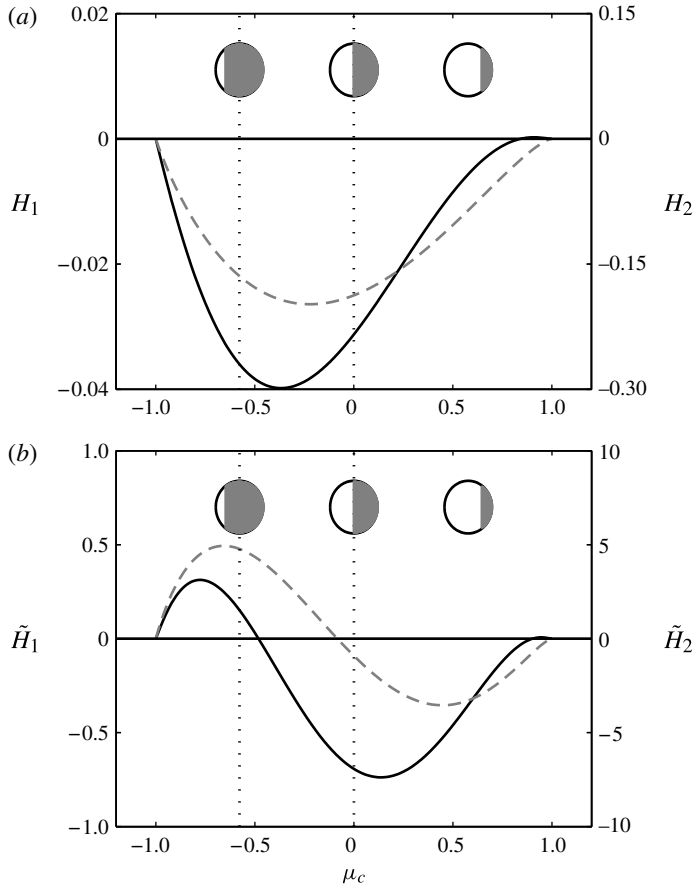
FIGURE 11. (*a*) Dependence on *Pe* and *Da* of the sensitivities H_1 (solid line) and H_2 (dashed line) of the swimming velocity magnitude for a Janus particle with $k(\mu) = 1_{[\mu_c, 1]}$ and positive mobility. (*b*) Evolution with *Pe* and *Da* of the sensitivities $\tilde{H}_1$ (solid line) and $\tilde{H}_2$ (dashed line) of the stresslet intensity for the same particle. Particles A and B are indicated by dotted lines.

but their dependence is non-symmetric with respect to $\mu_c = 0$, and two particles with reverse surface activity do not have the same sensitivity.

Since $H_2 < 0$ for all Janus particles, reactive effects always tend to reduce the velocity magnitude regardless of the sign of the mobility. This confirms our numerical observations in the previous section for particles A and B, and can actually be extended easily to any particle with a reactive 'stripe' rather than a reactive 'cap' (i.e. $k(\mu) = 1_{[\mu_c, \mu_u]}$). Reactive effects systematically reduce the solute consumption rate near the active surfaces, effectively penalizing the chemical activity of those regions by limiting the supply of fresh solute.

In contrast, (6.10) shows that the sensitivity of the autophoretic velocity to advective effects depends on the sign of the mobility *M*. For all Janus particles, regardless of the size μ_c of the active region, a positive (respectively, negative) mobility leads to a reduction (respectively, increase) in the velocity magnitude from advective effects. This extends to arbitrary μ_c our numerical results for particles A and B. When the

particle swims toward its reactive pole ($M > 0$), solute advection brings fluid of higher solute content closer to the reactive cap, reducing the contrast with the inert cap and the slip velocity magnitude. Instead, when the particle swims toward its inert pole ($M < 0$), advective effects increase the solute content near the front cap (the inert one) and concentrate the depleted region near the reactive pole, increasing the tangential solute gradients and the slip velocity.

6.2. *Asymptotic analysis for the stresslet*

Following a similar approach for the stresslet and linearizing equations (4.11)–(4.13) for the $p = 2$ mode, one obtains the asymptotic result

$$\Sigma = 4\pi M k_2 + Pe\, M^2 \tilde{H}_1 + Da\, M \tilde{H}_2 + o(Da, Pe), \tag{6.11}$$

with

$$\tilde{H}_1 = 10\pi \left[-\frac{k_1^2 + k_0 k_2}{30} + \frac{k_1 k_3}{112} + \sum_{n=2}^{\infty} \left(\frac{3n(n-2)k_n^2}{2(n+1)^2(2n-1)(2n+1)(2n+3)} \right. \right.$$
$$\left. \left. + \frac{3(3n-1)k_n k_{n+2}}{2(n+3)(2n+1)(2n+3)(2n+5)} \right) \right], \tag{6.12}$$

$$\tilde{H}_2 = -4\pi \sum_{n=0}^{\infty} \left[\frac{5n k_n^2}{(2n-1)(2n+1)(2n+3)} + \frac{15(n+2)^2 k_n k_{n+2}}{(2n+1)(2n+3)(2n+5)(n+3)} \right]. \tag{6.13}$$

This asymptotic result is, once again, in excellent agreement with the numerical results of §5 (figure 10). These results also emphasize the difference in the evolution of the stresslet for particles A and B. For particle A, $k_2 = 0$ and $\Sigma_0 = 0$, and the asymptotic form in (6.11) is consistent with the stresslet at finite Pe (and $Da = 0$) being negative regardless of the sign of the mobility (figure 3). When $Da \neq 0$, (6.11) also confirms that particles A of opposite mobility have stresslets of different sign (see figure 7).

When $\Sigma_0 \neq 0$ (e.g. particle B in §5), the relative sensitivity of the stresslet is obtained as

$$\left(\frac{1}{\Sigma} \frac{\partial \Sigma}{\partial Pe} \right)_{(Pe, Da)=(0,0)} = \frac{M \tilde{H}_1}{4\pi k_2}, \qquad \left(\frac{1}{\Sigma} \frac{\partial \Sigma}{\partial Da} \right)_{(Pe, Da)=(0,0)} = \frac{\tilde{H}_2}{4\pi k_2}. \tag{6.14a,b}$$

For generic Janus particles that have a finite stresslet in the reference configuration ($Pe = Da = 0$), (6.14) shows that increasing reactive effects (Da) will have the same influence on particles of opposite mobility, while increasing advective effects will lead to either a maximum stresslet at intermediate Pe or a monotonic decrease of Σ with Pe, consistent with figures 3 and 7 (note that the maximum in Σ for particle B is of very small amplitude).

Finally, it should be noted that the results of the asymptotic analysis in (6.7)–(6.9) and (6.11)–(6.13) are not restricted to Janus activity distributions but hold for any axisymmetric distribution of activity and could be used directly to investigate the sensitivity of a more general class of phoretic particles.

6.3. *Optimal Pe for arbitrary Janus particles*

The results in figure 11 suggest that the sensitivity to advective effects is strongly dependent on the extent of the reactive cap for an arbitrary Janus particle of negative mobility $M = -1$, and is non-symmetric with respect to $\mu_c = 0$. In particular, a maximum is reached for $\mu_c \approx -0.37$, with a sensitivity more than 25 % greater than the sensitivity to *Pe* of the symmetric particle A ($\mu_c = 0$). The sensitivity to advective effects tends to vanish in the limit of isotropic inert or active particles ($\mu_c \to \pm 1$). Further, when comparing the sensitivity of two symmetric particles, i.e. those with inverse cap-size ratio or, equivalently, opposite μ_c, the more reactive particle is always more sensitive to advective effects. As $U \to 0$ when $Pe \to \infty$ for all Janus particles, these results demonstrate the existence of an optimal *Pe* for $M < 0$ leading to a maximum velocity.

This observation is confirmed using nonlinear numerical simulations and by systematically varying μ_c and *Pe*. The results are shown in figure 12, where we display in panel (*a*) the iso-values of the phoretic velocity magnitude and plot in panel (*b*) the value of the maximum swimming velocity and corresponding optimal Péclet number as a function of the active cap size μ_c. Note that $Da = 0$ is chosen here since we identified a systematic penalization of the swimming velocity by reactive effects. The asymmetry between two symmetric particles P_1 and P_2 such that $k_{P_1}(\mu) = 1 - k_{P_2}(\mu)$ is apparent in figure 12. Advective effects are observed to significantly enhance the swimming velocity of particles with $\mu_c < 0$ (i.e. particles whose reactive cap is greater than the inert cap), while this effect is small for particles with smaller reactive caps ($\mu_c > 0$). This observation is consistent with a monotonic decrease with μ_c of the optimal Péclet number, Pe_M, at which the maximum velocity is achieved. A mostly inert particle will experience a small peak velocity for low *Pe*, while mostly active particles will experience a large velocity increase for $Pe \gtrsim 1$–10.

The limit $\mu_c \to -1$ is particularly intriguing. This corresponds to an almost fully reactive particle except for a very small inert cap near the left pole. Such particles do not experience any significant self-propulsion at $Pe = 0$; however, figure 12 shows that such a particle may achieve a finite propulsion velocity for large *Pe*. Michelin *et al.* (2013) showed that the completely reactive particle ($\mu_c = -1$) may achieve self-propulsion at finite *Pe* despite spherical symmetry, through an instability and symmetry-breaking process arising from the nonlinear coupling of the solute dynamics and phoretic slip velocity near the surface of the particle. The mechanism leading to self-propulsion at high *Pe* has the same origin. More precisely, the dependence of $|U|$ on *Pe* appears to converge asymptotically to that obtained for the isotropic reactive particle as $\mu_c \to -1$ (figure 13). Infinitesimal velocities are obtained below the instability threshold $Pe = 4$ (see the derivation in Michelin *et al.* 2013) and are solely due to the symmetry-breaking introduced by the presence of a small inert cap on the left. Beyond $Pe = 4$, the instability resulting from the nonlinear coupling of the surface phoretic flows and solute advection–diffusion dominates and leads to finite swimming velocity.

Finally, the dependence of the stresslet intensity, Σ, with *Pe* and μ_c also exhibits asymmetry, as shown in figure 14. At small *Pe*, the sign of μ_c determines the sign of the stresslet. In the case of negative mobility, $M = -1$, mostly reactive particles behave as pullers ($\mu_c < 0$, $\Sigma > 0$), while mostly inert particles behave as pushers ($\mu_c > 0$, $\Sigma < 0$). The conclusions are reversed for $M = 1$. At intermediate and large *Pe*, this symmetry around $\mu_c = 0$ no longer holds and particles with a reactive cap slightly larger than a hemisphere may experience a change in sign of their stresslet intensity, becoming pushers at large *Pe*. For such particles, the maximum stresslet, resulting
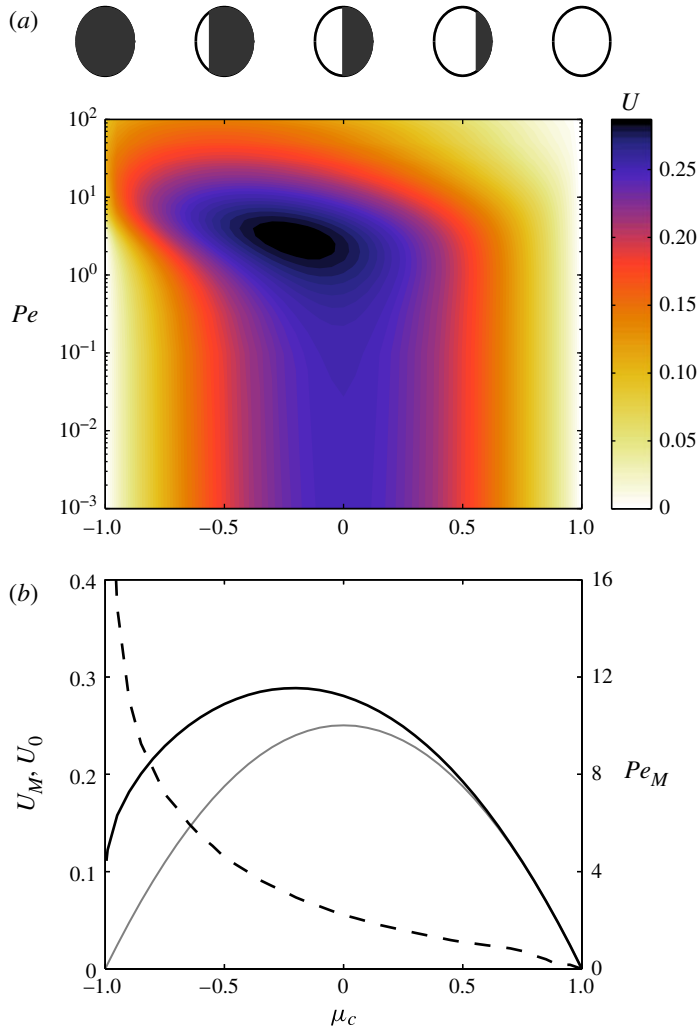
FIGURE 12. (Colour online) (*a*) Dependence of the phoretic velocity magnitude on *Pe* and the relative size of the reactive cap, μ_c (see illustration at the top); $\mu_c = -1$ corresponds to a fully reactive particle and $\mu_c = 1$ corresponds to a fully inert particle. All reactive effects are neglected ($Da = 0$) and negative mobility $M = -1$ is considered, so the particles swim to the left. (*b*) Dependence on μ_c of the optimal Péclet number Pe_M (dashed line), leading to the maximum velocity U_M (black solid line), and of the self-propulsion velocity in the absence of advective effects, U_0 ($Pe = 0$, grey solid line).

in the strongest interparticle interaction, is obtained at large *Pe*. Results obtained for $M = 1$ (not shown here) exhibit the same dominance of the pusher characteristic: particles with $\mu_c > 0$, which are pullers at $Pe = 0$, become pushers at larger *Pe*.

7. Conclusions

Our work generalizes the classical continuum phoretic framework to account for finite advective and reactive effects. Our results highlight the influence of such effects on the self-propulsion of axisymmetric Janus particles, and are relevant to phoretic
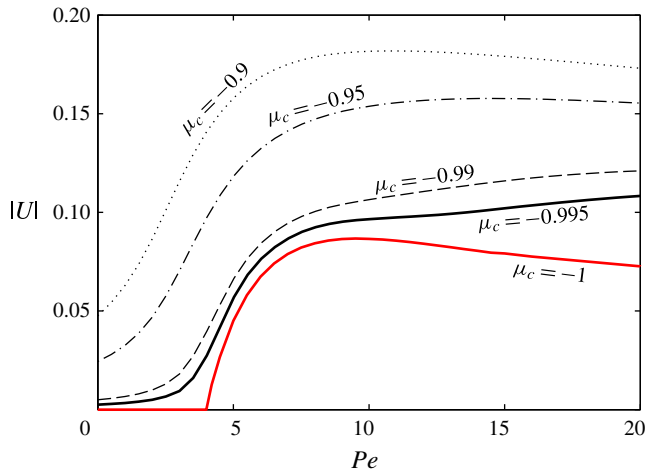
FIGURE 13. (Colour online) Dependence of the velocity magnitude $|U|$ on the Péclet number Pe, for Janus particles with $\mu_c = -0.9$ (dotted line), $\mu_c = -0.95$ (dash–dotted line), $\mu_c = -0.99$ (dashed line) and $\mu_c = -0.995$ (thin solid line) with negative mobility. The velocity obtained for a strictly isotropic particle with $\mu_c = 1$ and resulting from a symmetry-breaking instability (Michelin *et al.* 2013) is shown as a thick solid (red) line.

particles of sufficiently large radius. In particular, advection of the solute by the phoretic flows can lead to significant increases in the swimming velocity, which may reach a maximum at a finite, order-one value of the Péclet number. When the surface chemistry corresponds to solute consumption at the particle boundary, such a peak in the self-propulsion velocity is observed only for particles of negative mobility (corresponding to locally attractive solute–surface interactions), while particles of positive mobility experience a monotonic decrease of their propulsion velocity with Pe. The impact of the geometrical active-versus-inert coverage of the particle surface was also identified. Particles that are predominantly reactive are more sensitive to advective effects and experience the largest increase in their swimming velocity at finite Pe, whereas such effects are almost negligible for predominantly inert particles.

In contrast, reactive effects always penalize the self-propulsion of Janus phoretic particles in all situations: when reaction acts too rapidly for the solute diffusion to refresh the solute content in the vicinity of the particle, the rate of consumption of the solute at the surface is reduced, effectively amounting to a reduction of surface activity that decreases the slip velocity and hence penalizes self-propulsion.

Notably, the situation in which we predict locomotion to be enhanced by advection effects (finite value of Pe) is that of the system recently considered in a number of experimental investigations (Howse *et al.* 2007; Ebbens & Howse 2011; Ebbens *et al.* 2012). In this set-up, polymeric particles half-coated with platinum are used to catalyse the autodegradation of hydrogen peroxide, H_2O_2, into dioxygen, O_2. Self-diffusiophoresis due to the action of O_2 gradients corresponds to net locomotion with the polymeric side of the particle first: $k < 0$ and $M > 0$. This situation is equivalent to the case of $k > 0$ and $M < 0$ computed above, and for which we predict locomotion to be enhanced by solute advection. Past experiments with this system have a Péclet number that is too small by about one order of magnitude for the effect to have been observed yet, but it could play a role in the case of larger particles. The effect also certainly plays an important role in the case of motion driven by surfactant gradients
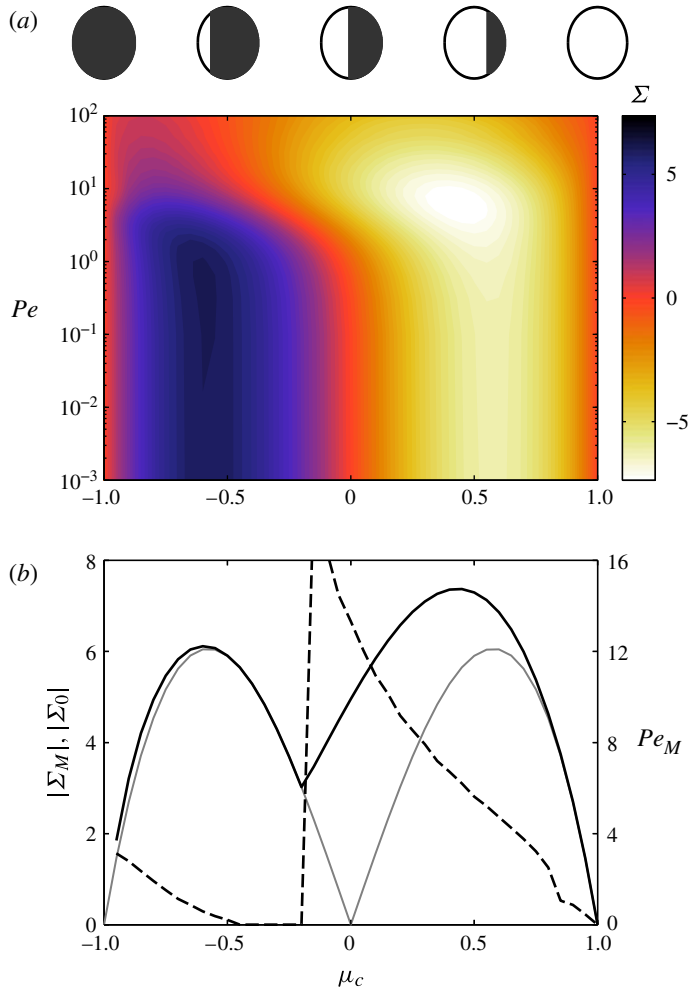
FIGURE 14. (Colour online) (*a*) Dependence of the stresslet intensity Σ on *Pe* and μ_c, the relative size of the reactive cap. All reactive effects are neglected ($Da = 0$) and negative mobility $M = -1$ is considered (so that swimming occurs to the left). (*b*) Dependence on μ_c of the optimal Péclet number Pe_M (dashed line), leading to a maximum stresslet magnitude $|\Sigma_M|$ (black solid line), and of the stresslet magnitude in the absence of advective effects, $|\Sigma_0|$ ($Pe = 0$, grey solid line).

where, due to much smaller molecular diffusivity, Péclet numbers can easily reach $O(100)$ (Thutupalli *et al.* 2011).

   In this paper, we have chosen to concentrate exclusively on propulsion through self-diffusiophoresis of a particle, which catalyses a simple one-step chemical reaction $S \rightarrow \emptyset$ on its surface. This framework can easily be extended to account for situations where both reagents and products of the reaction interact significantly with the surface or where there are multiple-step reactions (e.g. see Ebbens *et al.* 2012). More generally, the results of our study are likely to remain valid for other phoretic mechanisms, provided the particle possesses two properties, namely mobility and activity. The former characterizes the ability of the particle to generate a slip velocity from an external field modified by advection and diffusion, while the latter

corresponds to the particle's ability to create local gradients of this field through chemical reaction or heat absorption/release (e.g. Jiang *et al.* 2010; Bickel, Majee & Würger 2013).

Reactive and advective effects not only modify propulsion velocities but also significantly affect the flow field created by the particles and are therefore expected to modify the type and intensity of hydrodynamic interactions between neighbouring particles. The collective dynamics of such colloid particles was shown recently to exhibit different complex behaviours (Theurkauff *et al.* 2012; Palacci *et al.* 2013). A complete fundamental understanding of the mechanisms leading to such aggregation and collective organization remains to be developed. Nevertheless, the results presented in this work suggest that for larger particles, advective and, to a smaller extent, reactive effects may be significant.

Finally, the results obtained here rely on the assumption of a thin interaction layer, considered in most existing literature. We have carefully identified the conditions under which this assumption and the resulting framework are valid, namely when advection within the interaction layer can be neglected. The generalization of these results to the limit of very large *Pe* (i.e. when $\varepsilon Pe = O(1)$ or above) remains an open question. Depending on the nature of the solute–particle interaction, advection within the interaction layer may enhance or reduce the local solute gradients, respectively increasing or penalizing the self-propulsion velocity. Another interesting question to consider would be the effect of interactions between solute molecules, effectively introducing variations of the interaction potential with the solute concentration.

Appendix A. Generalization to non-uniform mobility

The framework and results presented in the main part of the paper can easily be extended to the case of a particle with non-uniform mobility, which may be more relevant to experimental conditions. Indeed, the chemical treatment of the surface of the particle is likely to affect both surface activity and mobility. From a theoretical point of view, the phoretic problem formulation in (4.1)–(4.5) remains valid for non-uniform $M(\mu)$. Its formulation in the squirmer framework is only marginally modified; while (4.11)–(4.13) remain unchanged, (4.14) must be replaced by

$$\alpha_n = - \sum_{m,p=0}^{\infty} \frac{n(n+1)}{(2n+1)(2p+1)} M_p c_m(1) B_{mnp}, \tag{A 1}$$

with B_{mnp} as defined in (4.16) and $M(\mu) = \sum M_p L_p(\mu)$. We briefly show here that the results presented in the main part of the paper remain valid when non-uniform mobility is considered, focusing on the configuration $M(\mu) = \pm k(\mu)$ (the chemical patterning of the particle surface affects both properties at the same time).

Figure 15 displays the dependence of the swimming velocity of the particle on *Pe* and the surface chemical coverage, and thus generalizes the results of figure 12 to the case of non-uniform mobility. The swimming velocity levels are generally obviously reduced, since a smaller fraction of the particle contributes to the slip velocity, but the main conclusions of the paper are unchanged. Specifically, in the case of negative mobility, there exists an optimal $Pe(\mu_c)$ maximizing the swimming velocity. Further, this advective effect is more pronounced for particles whose reactive cap is greater than a hemisphere ($\mu_c < 0$). The analysis obtained for $\mu_c \rightarrow -1$ is also strictly equivalent to the uniform mobility case: in that limit, the existence of a small cap with zero mobility near the left pole does not modify the swimming
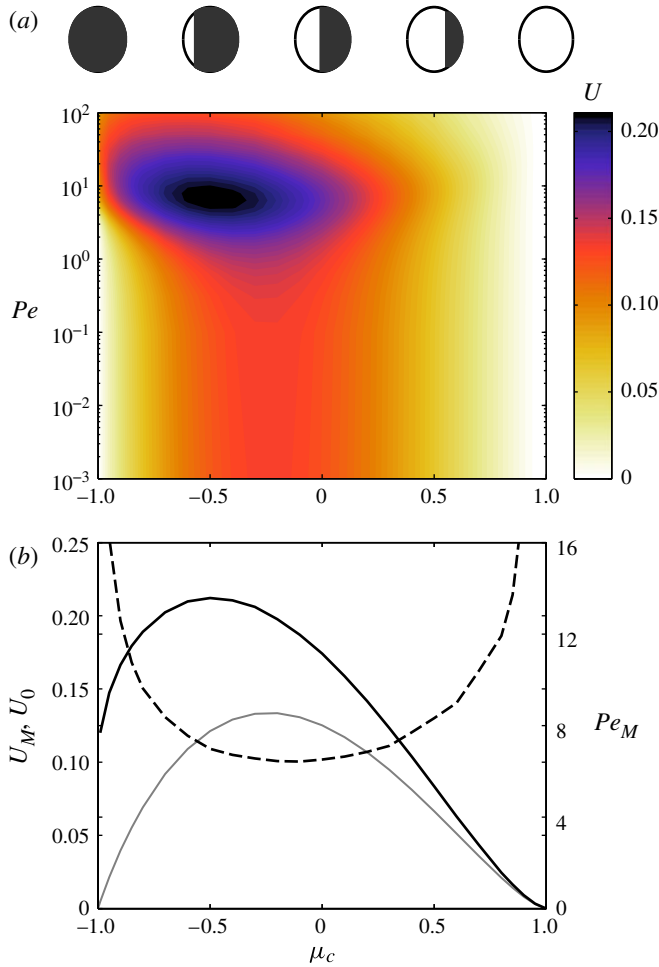
FIGURE 15. (Colour online) Same results as figure 12 but for a particle with non-uniform mobility, $M(\mu) = -k(\mu)$. (a) Dependence of the phoretic velocity magnitude on Pe and μ_c, the relative size of the reactive cap. Reactive effects are neglected ($Da = 0$) and negative mobility $M(\mu) = -k(\mu)$ is considered (so that swimming is to the left). (b) Dependence on μ_c of the optimal Péclet number Pe_M (dashed line), leading to the maximum velocity U_M (black solid line), and of the self-propulsion velocity in the absence of advective effects, U_0 ($Pe = 0$, grey solid line).

velocity significantly, since it corresponds to a small surface and the slip velocity in that region is almost orthogonal to the swimming direction.

   These results differ from those in the main part of the paper only in two minor points: the swimming velocity at $Pe = 0$ is no longer symmetric with respect to $\mu_c = 0$, and the optimal Pe for $\mu_c \to 1$ is large instead of converging to zero. The former is a consequence of the greater surface contributing to the swimming velocity when $\mu_c < 0$ compared with when $\mu_c > 0$. The latter indicates that the optimal velocity is reached for large Pe. However, as for the configuration with uniform mobility, this optimal velocity differs only marginally from the reference velocity U_0, and such Janus particles are still only weakly sensitive to advective effects. Finally, we note

that for non-uniform mobility, advective effects can lead to stronger increases in the swimming velocity.

REFERENCES

ANDERSON, J. L. 1989 Colloid transport by interfacial forces. *Annu. Rev. Fluid Mech.* **21**, 61–99.

ANDERSON, J. L. & PRIEVE, D. C. 1991 Diffusiophoresis caused by gradients of strongly adsorbing solutes. *Langmuir* **7**, 403–406.

BATCHELOR, G. K. 1970 The stress system in a suspension of force-free particles. *J. Fluid Mech.* **41**, 545–570.

BENDER, C. M. & ORSZAG, S. A. 1978 *Advanced Mathematical Methods for Scientists and Engineers*. McGraw-Hill.

BICKEL, T., MAJEE, A. & WÜRGER, A. 2013 Flow pattern in the vicinity of self-propelling hot Janus particles. *Phys. Rev.* E **88**, 012301.

BLAKE, J. R. 1971 A spherical envelope approach to ciliary propulsion. *J. Fluid Mech.* **46**, 199–208.

BRADY, J. 2011 Particle motion driven by solute gradients with application to autonomous motion: continuum and colloidal perspectives. *J. Fluid Mech.* **667**, 216–259.

BRAY, D. 2000 *Cell Movements: From Molecules to Motility*. Garland Science.

BRENNEN, C. & WINNET, H. 1977 Fluid mechanics of propulsion by cilia and flagella. *Annu. Rev. Fluid Mech.* **9**, 339–398.

BROYDEN, C. G. 1965 A class of methods for solving nonlinear simultaneous equations. *Maths Comput.* **19**, 577–593.

CÓRDOVA-FIGUEROA, U. M. & BRADY, J. F. 2008 Osmotic propulsion: the osmotic motor. *Phys. Rev. Lett.* **100** (15), 158303; see also the comment on this article by F. Jülicher & J. Prost, *Phys. Rev. Lett.* **103**, 079801.

CÓRDOVA-FIGUEROA, U. M., BRADY, J. F. & SHKLYAEV, S. 2013 Osmotic propulsion of colloidal particles via constant surface flux. *Soft Matt.* **9**, 6382–6390.

DREYFUS, R., BAUDRY, J., ROPER, M. L., FERMIGIER, M., STONE, H. A. & BIBETTE, J. 2005 Microscopic artificial swimmers. *Nature* **437**, 862–865.

EBBENS, S. J. & HOWSE, J. R. 2011 Direct observation of the direction of motion for spherical catalytic swimmers. *Langmuir* **27**, 12293–12296.

EBBENS, S., TU, M.-H., HOWSE, J. R. & GOLESTANIAN, R. 2012 Size dependence of the propulsion velocity for catalytic Janus-sphere swimmers. *Phys. Rev.* E **85**, 020401.

GAO, W., SATTAYASAMITSATHIT, S., MANESH, K. M., WEIHS, D. & WANG, J. 2010 Magnetically powered flexible metal nanowire motors. *J. Am. Chem. Soc.* **132**, 14403–14405.

GHOSH, A. & FISCHER, P. 2009 Controlled propulsion of artificial magnetic nanostructured propellers. *Nano Lett.* **9**, 2243–2245.

GOLESTANIAN, R., LIVERPOOL, T. B. & AJDARI, A. 2005 Propulsion of a molecular machine by asymmetric distribution of reaction products. *Phys. Rev. Lett.* **94** (22), 220801.

GOLESTANIAN, R., LIVERPOOL, T. B. & AJDARI, A. 2007 Designing phoretic micro- and nano-swimmers. *New J. Phys.* **9**, 126.

HOWSE, J. R., JONES, R. A. L., RYAN, A. J., GOUGH, T., VAFABAKHSH, R. & GOLESTANIAN, R. 2007 Self-motile colloidal particles: from directed propulsion to random walk. *Phys. Rev. Lett.* **99**, 048102.

JIANG, H.-R., YOSHINAGA, N. & SANO, M. 2010 Active motion of a Janus particle by self-thermophoresis in a defocused laser beam. *Phys. Rev. Lett.* **105**, 268302.

JÜLICHER, F. & PROST, J. 2009*a* Comment on osmotic propulsion: the osmotic motor. *Phys. Rev. Lett.* **103**, 079801.

JÜLICHER, F. & PROST, J. 2009*b* Generic theory of colloidal transport. *Eur. Phys. J.* E **29** (1), 27–36.

KHAIR, A. S. 2013 Diffusiophoresis of colloidal particles in neutral solute gradients at finite Péclet number. *J. Fluid Mech.* **731**, 64–94.

LAUGA, E. & POWERS, T. R. 2009 The hydrodynamics of swimming micro-organisms. *Rep. Prog. Phys.* **72**, 096601.

MAGAR, V., GOTO, T. & PEDLEY, T. J. 2003 Nutrient uptake by a self-propelled steady squirmer. *Q. J. Mech. Appl. Maths* **56**, 65–91.

MICHELIN, S. & LAUGA, E. 2011 Optimal feeding is optimal swimming for all Péclet numbers. *Phys. Fluids* **23** (10), 101901.

MICHELIN, S. & LAUGA, E. 2013 Unsteady feeding and optimal strokes of model ciliates. *J. Fluid Mech.* **715**, 1–31.

MICHELIN, S., LAUGA, E. & BARTOLO, D. 2013 Spontaneous autophoretic motion of isotropic particles. *Phys. Fluids* **25**, 061701.

NELSON, B. J., KALIAKATSOS, I. K. & ABBOTT, J. J. 2010 Microrobots for minimally invasive medicine. *Annu. Rev. Biomed. Engng* **12** (1), 55–85.

O'BRIEN, R. W. 1983 The solution of the electrokinetic equations for colloidal particles with thin double layers. *J. Colloid Interface Sci.* **92**, 204–216.

PALACCI, J., SACANNA, S., STEINBERG, A. P., PINE, D. J. & CHAIKIN, P. M. 2013 Living crystals of light-activated colloidal surfers. *Science* **339**, 936–940.

PAXTON, W. F., KISTLER, K. C., OLMEDA, C. C., SEN, A., ANGELO, S. K. ST., CAO, Y., MALLOUK, T. E., LAMMERT, P. E. & CRESPI, V. H. 2004 Catalytic nanomotors: autonomous movement of striped nanorods. *J. Am. Chem. Soc.* **126** (41), 13424–13431.

POPESCU, M. N., DIETRICH, S., TASINKEVYCH, M. & RALSTON, J. 2010 Phoretic motion of spheroidal particles due to self-generated solute gradients. *Eur. Phys. J.* E **31**, 351–367.

PRIEVE, D. C., ANDERSON, J. L., EBEL, J. P. & LOWELL, M. E. 1984 Motion of a particle generated by chemical gradients. Part 2. Electrolytes. *J. Fluid Mech.* **148**, 247–269.

PURCELL, E. M. 1977 Life at low Reynolds number. *Am. J. Phys.* **45**, 3–11.

SABASS, B. & SEIFERT, U. 2012 Dynamics and efficiency of a self-propelled, diffusiophoretic swimmer. *J. Chem. Phys.* **136**, 064508.

SCHMITT, M. & STARK, H. 2013 Swimming active droplet: a theoretical analysis. *Eur. Phys. Lett.* **101**, 44008.

SHARIFI-MOOD, N., KOPLIK, J. & MALDARELLI, C. 2013 Diffusiophoretic self-propulsion of colloids driven by a surface reaction: the sub-micron particle regime for exponential and van der Waals interactions. *Phys. Fluids* **25**, 012001.

STONE, H. A. & SAMUEL, A. D. T. 1996 Propulsion of microorganisms by surface distorsions. *Phys. Rev. Lett.* **77**, 4102.

THEURKAUFF, I., COTTIN-BIZONNE, C., PALACCI, J., YBERT, C. & BOCQUET, L. 2012 Dynamic clustering in active colloidal suspensions with chemical signaling. *Phys. Rev. Lett.* **108**, 268303.

THUTUPALLI, S., SEEMANN, R. & HERMINGHAUS, S. 2011 Swarming behaviour of simple model squirmers. *New J. Phys.* **13**, 073021.

WALTHER, A. & MÜLLER, A. H. E. 2008 Janus particles. *Soft Matt.* **4**, 663–668.

WANG, J. 2009 Can man-made nanomachines compete with nature biomotors? *ACS Nano* **3**, 4–9.

YARIV, E. 2010 An asymptotic derivation of the thin-Debye-layer limit for electrokinetic phenomena. *Chem. Engng Commun.* **197**, 3–17.

YOSHINAGA, N., NAGAI, K. H., SUMINO, Y. & KITAHATA, H. 2012 Drift instability in the motion of a fluid droplet with a chemically reactive surface driven by Marangoni flow. *Phys. Rev.* E **86**, 016108.

ZHANG, L., PEYER, K. E. & NELSON, B. J. 2010 Artificial bacterial flagella for micromanipulation. *Lab on a Chip* **10**, 2203–2215.